

©Climatologies of Mesoscale Convective Systems over China Observed by Spaceborne Radars

HAO CHEN,^a WEIXIN XU,^{a,b,c} NANA LIU,^d JIANHUA SUN,^{b,e} AND JIAOLAN FU^f

^a Sun Yat-Sen University, Zhuhai, China

^b Southern Marine Science and Engineering Guangdong Laboratory (Zhuhai), Zhuhai, China

^c Guangdong Province Key Laboratory for Climate Change and Natural Disaster Studies, Guangzhou, China

^d Department of Earth System Science, University of California, Irvine, Irvine, California

^e Institute of Atmospheric Physics, Chinese Academy of Sciences, Beijing, China

^f National Meteorological Center, China Meteorological Administration, Beijing, China

(Manuscript received 21 December 2021, in final form 27 June 2022)

ABSTRACT: This study investigates the characteristics of mesoscale convective systems (MCSs) as a function of MCS organizational mode over China, using long-term precipitation radar observations from the Tropical Rainfall Measuring Mission (TRMM) and Global Precipitation Measurement Mission (GPM). The spaceborne radar-based MCS climatology shows maximum population over low-elevation regions, marked decrease over the foothills, and minimum frequency over the Tibetan Plateau. Linear and nonlinear MCSs account for 17% and 83% of the MCSs over China, respectively. Linear MCSs have much stronger convective intensity and heavier precipitation than nonlinear MCSs, as indicated by TRMM convective proxies. Interestingly, though broad-stratiform MCSs have the weakest convection, they produce the heaviest (maximum) rain rate and the largest amount of heavy rainfall among nonlinear MCSs. Among various types of linear MCSs, bow echoes (BEs) and no-stratiform (NS) systems exhibit the strongest convective intensity, embedded lines exhibit the weakest, and convective lines with trailing/leading stratiform in between. BEs and NSs share the most vertically extended structure, strongest microwave ice scattering, and highest lightning flash rates, but NS systems have a much lower surface rain rate likely due to a drier environment. Vertical radar reflectivity profiles suggest that both ice-based and warm-rain processes play an important role in the precipitation processes of linear MCSs over China, including the most intense BE storms. In short, this study helps to better understand the convective organization, precipitation structure, and ensemble microphysical properties of MCSs over China, and potentially provides guidelines for evaluating high-resolution model simulations and satellite rainfall retrievals for monsoonal MCSs.

KEYWORDS: Convective storms/systems; Mesoscale systems; Precipitation; Squall lines; Radars/Radar observations

1. Introduction

Mesoscale convective systems (MCSs), typically hundreds of kilometers in the horizontal scale, are organized regions of deep convection. They not only frequently induce severe weathers such as flooding, damaging wind, and large hail, but also significantly contribute to the total rainfall around the world (Nesbitt et al. 2006; Houze 2018; Schumacher and Rasmussen 2020; Feng et al. 2021). Under the climate warming recorded during the past several decades, MCSs over both the central United States and West African Sahel have been found to occur more frequently and to exhibit trends toward stronger, more extended, and longer-lived systems (Feng et al. 2016; Taylor et al. 2017; Prein et al. 2017; Houze 2018; Rasmussen et al. 2020). In turn, MCS can affect the large-scale circulations by redistributing momentum, heat, and moisture (Stensrud 1996; Schumacher and Johnson 2005; Moncrieff 2010; Liu et al. 2015). MCSs have been a hot research topic worldwide (summarized in Houze 2018 and Schumacher and Rasmussen 2020). They can be

generally categorized by linear (e.g., squall line) and nonlinear organizations such as near-circular convective systems (Houze 2018; Schumacher and Rasmussen 2020). Squall lines have been shown to be responsible for much of the short-duration heavy rainfall, flash floods, large hail, and even tornadoes (Houze et al. 1990; Schumacher and Johnson 2006; Stevenson and Schumacher 2014; Cecil and Blankenship 2012). The type and severity of severe weather on the organizational mode of squall lines (Parker and Johnson 2000; X. Wang et al. 2014; Zheng et al. 2013; Ma et al. 2021). For instance, squall lines organized as convective lines with leading stratiform or trailing stratiform precipitation are more likely to induce hail and tornado threat (Gallus et al. 2008), whereas bow echo systems are more favorable for damaging winds or derechos (Schenkman and Xue 2016; Guastini and Bosart 2016; Xia et al. 2012; Weisman 1993).

MCSs are quite frequent over China and contribute 40%–50% of the total rainfall in most regions, especially in the lower-elevation areas (Li et al. 2020). Nearly half of the heavy rainfall events are associated with MCSs in eastern China, and up to 80% over areas along the Yangtze River valley (He et al. 2016; Zhang et al. 2019). In addition, MCSs frequently induce strong wind and damaging hail (Zhang et al. 2008; Xie et al. 2010; Zheng et al. 2013; Yang and Sun 2018), and sometimes even produce tornados (Meng et al. 2018).

© Denotes content that is immediately available upon publication as open access.

Corresponding author: Weixin Xu, xuwx25@mail.sysu.edu.cn

MCSs over China have been extensively investigated, based on satellite infrared (IR) measurements, rain gauge-satellite combined data, and ground-based radar observations. IR-based studies reported three MCS maxima in China, occurring over South China (southernmost China), Yangtze River valley (central-eastern China), and Tibetan Plateau (Zheng et al. 2008; Yang et al. 2015; Chen et al. 2019; Cui et al. 2020). Over South China, MCSs frequently develop along either cold fronts in April or quasi-stationarity fronts during the mei-yu season in May–June (Sun and Zhang 2012; Yang et al. 2015; Cui et al. 2020). Orographic enhancement may also play a role in triggering/enhancing MCSs and heavy precipitation in South China (Du et al. 2020; H. Wang et al. 2014). MCSs over the Yangtze River valley are often associated with active mei-yu fronts during June–July (Yang et al. 2015; Chen et al. 2019; Cui et al. 2020; Li et al. 2020). Some MCSs originate over the second-step terrain just east of the Tibetan Plateau and propagate eastward into the plains or coastal regions in eastern China (Ding and Chan 2005; Yang et al. 2018; Mai et al. 2021; Meng et al. 2021). This is similar to summertime MCSs over the continental United States (CONUS), which frequently initiate on the lee side of the Rocky Mountains and propagate eastward into the Great Plains (Carbone and Tuttle 2008; Zhang et al. 2014; Feng et al. 2019). Another warm-season MCS maximum is reported over the southern Tibetan Plateau by IR measurements (Zheng et al. 2008; Mai et al. 2021; Meng et al. 2021; Zhang et al. 2021). However, it is uncertain whether these MCSs produce significant rainfall at surface or mainly thick, cold clouds, given the poor relationship between IR brightness temperature and the surface precipitation (Arkin and Meisner 1987; Rickenbach 1999). Though continuous satellite IR observations provide important information about the evolution and propagation of MCSs (Yang et al. 2015; Ai et al. 2016), details about the partitioning between convective and stratiform rain areas, as well as the vertical structure of MCSs are unknown from the IR-based MCS climatologies.

Many studies have examined organizational characteristics of MCSs over China (mainly east and north China), especially linear MCSs (squall lines) using ground-based radar measurements (Meng et al. 2013; Zheng et al. 2013; Zhang et al. 2019; Yang and Sun 2018; Liu et al. 2021; Ma et al. 2021). Meng et al. (2013) identified 96 intense squall lines over eastern China from 2008 to 2009, which tend to be the strongest over coastal regions and the weakest over the mountainous areas. They further found that certain synoptic patterns are more favorable for squall lines such as pre-trough, cold vortex, subtropical high, tropical cyclone, and post-trough. The organizational modes of squall lines were also documented over the central Eastern China, the Yangtze River basin, and the North China based on operational radars, and attributed to various forms of severe weather (Zheng et al. 2013; X. Wang et al. 2014; Liu et al. 2021). Over 70% of the trailing-stratiform MCSs over central-eastern China produce heavy rainfall ($>20 \text{ mm h}^{-1}$), while extreme precipitation ($>50 \text{ mm h}^{-1}$) is the most frequent in parallel-stratiform MCSs (Zheng et al. 2013). Over North China, severe winds ($>17 \text{ m s}^{-1}$) over the plains are frequently produced by squall lines, whereas they are more connected to

isolated convective clusters over the mountains (Yang and Sun 2018). Though the abovementioned studies found many interesting features of linear MCSs in China, they mainly focused on intense MCSs (e.g., inducing severe wind or hail) but knowledge about their spatiotemporal coverage is relatively limited. Moreover, ground-based radar measurements may be subject to severe beam blockage issues over hill areas in southeast China (Meng et al. 2013) and complex terrain in the western parts of China.

Compared to the MCS horizontal structure, the vertical structure of MCSs in China are less known. Results based on nearly 10 years of TRMM precipitation radar measurements showed significant regional and intraseasonal variations in the vertical structure of MCSs in China (Xu et al. 2009; Luo et al. 2013). During the active monsoon periods, MCSs over the Yangtze River exhibit significantly higher radar echo-top heights than those over South China (Luo et al. 2013). Interestingly, MCSs have stronger radar vertical profiles (e.g., higher reflectivity) prior to the onset of the mei-yu season than the active mei-yu periods (Xu et al. 2009). Similar intraseasonal variations in the vertical structure of MCS over the coastal South China are also reported using ground-based radar measurements (Chen et al. 2014). Recently, Sun et al. (2020) found that the vertical structure of stratiform precipitation in MCSs associated with mei-yu fronts are similar to those over the ocean due to high relative humidity. They also reported significant variations in the vertical structure and microphysics of convective cores during various mei-yu MCS stages. However, the vertical structure and ensemble microphysical properties of MCSs in China (especially squall lines) are rarely investigated as a function of organizational mode, which is important for evaluating MCS structure and microphysical parameterization in high-resolution models.

The long-term global precipitation radar observations from the Tropical Rainfall Measuring Mission (TRMM) and the Global Precipitation Measurement Mission (GPM) satellites are uniquely beneficial for studying convective climatology (Nesbitt et al. 2000; Zipser et al. 2006; Houze et al. 2007; Houze et al. 2015; Houze 2018). More importantly, spaceborne radars have minimum beam-blocking issues by “looking” down from the space and thus they are superior to ground-based radars in observing convection over complex terrain. This study makes use of this powerful tool to comprehensively investigate the MCS climatologies over China. Particularly, general MCS climatologies over East Asia including China will be discussed in section 3, and section 4 will compare linear and nonlinear MCSs over China. Section 5 will focus on squall lines over China, including their organization modes, environmental conditions, convective characteristics, and vertical structure.

2. Data and methodology

a. Gridding TRMM and GPM pixel data

Satellite data used in this study include observations from the precipitation radar (PR), Microwave Imager (TMI), and Lightning Imaging Sensor (LIS) on board the TRMM satellite,

and the GPM dual frequency precipitation radar (DPR). Both the Ku-band radars of PR and DPR may subject to attenuation issue especially by heavy precipitation, which has been well corrected through advanced attenuation correction algorithm (Iguchi et al. 2000; Seto and Iguchi 2015). Compared to ground-based radars, spaceborne radars (PR and DPR) look down directly from the space, therefore, they should have minimum influences (e.g., radar beam blockage) from complex terrain. Ground clutter and sidelobe effects have been sufficiently corrected (Iguchi et al. 2000, 2021). Also, artificial strong reflectivities near the surface of some steep terrain in V07 PR data (Hamada and Takayabu 2014) had been corrected in V08 (Wang and Tang 2020). Though there may be still certain uncertainties in the near-surface radar reflectivity or precipitation estimation, PR and DPR measurements are supposed to be the best-available radar data over complex terrain (Nesbitt and Anders 2009; Houze et al. 2015).

TRMM samples from 35°S to 35°N, and GPM's sampling extends to 65°S to 65°N. The observations from TRMM and GPM are available from 1998 to 2014 and from 2014 to 2019, respectively. The TRMM/GPM orbital data, with original horizontal resolutions ranging from 5 to 8 km, are remapped to the Cartesian coordinate with a horizontal resolution of 0.05° and vertical resolution of 250 m, using the closest point interpolating method. The areal-mean rain rates ($1^\circ \times 1^\circ$) in 1998–2018 are derived by averaging the near-surface precipitation data from both the TRMM and GPM precipitation radars. The original UTC times in TRMM/GPM data are adapted to local time (LT) using the time and longitude information of specific grids. That is, $T_{\text{local}} = [T_{\text{UTC}} + \text{lon} \times (24/360)] \bmod 24$, where T_{local} and T_{UTC} are the LT and UTC, respectively, and lon is longitude.

b. MCS identification and categorization

MCSs are identified based on the gridded TRMM PR and GPM DPR data. The flowchart of the identification procedures and algorithms are shown in the appendix (see Fig. A1). Contiguous raining grids (rain rate $> 0.1 \text{ mm h}^{-1}$) at the near surface are first clustered as echo objects using an elliptical fitting method similar to the TRMM precipitation feature (Nesbitt et al. 2000; Liu et al. 2008). An MCS is then defined as an echo object satisfying the following conditions: 1) major axis (of the fitting ellipse) greater than 100 km, 2) total areas of convective rain larger than 900 km^2 (not necessarily continuous), and 3) maximum near-surface reflectivity reaching at least 40 dBZ. Identified MCSs are categorized as either linear or nonlinear. Linear MCSs are subjectively identified based on the linear organization of the convective areas (PR/DPR convective precipitation type), following previous studies (Meng et al. 2013; Parker and Johnson 2000; Zheng et al. 2013). Specifically, the convective region of linear MCSs meets the following criteria: 1) contiguous 35-dBZ areas with the longest dimension greater than 75 km, 2) the ratio of shorter dimension to the longer dimension of the convective region < 0.3 , 3) a quasi-contiguous 40-dBZ band is embedded within the convective region. Note that the intensity criterion (quasi-contiguous 40-dBZ band) is the same as Parker and Johnson (2000),

but slightly lower than Meng et al. (2013), which focused on strong squall lines with strictly contiguous 40-dBZ band. MCSs that fail to meet the aforementioned criteria are classified as nonlinear.

Linear MCSs are further divided into five organizational modes based on the shape of the convective region and the arrangement of the stratiform precipitation region, namely, trailing stratiform (TS), leading stratiform (LS), parallel stratiform (PS), bow echo (BE), no stratiform (NS), and embedded line (EL). These organizational modes are identified subjectively following rules outlined in previous studies (Zheng et al. 2013; Ma et al. 2021; Gallus et al. 2008; Parker and Johnson 2000). Examples of various linear MCS modes are shown in the appendix (see Fig. A2). TS and LS are convective lines having a trailing/leading stratiform precipitation region, respectively. Since the MCS moving direction is unable to be determined by the TRMM/GPM snapshots, the TS and LS are classified into the same group. BEs have similar convective organization as TS and LS, except that their convective line is in a bow shape. EL is characterized as a convective line embedded in the stratiform precipitation, whose maximum widths on both sides of the convective region are wider than that of the convective line. NS is defined as convective line having little stratiform precipitation at both the leading and trailing edges of the line. As far as PS, at least one-third of the convective line has little stratiform precipitation, while the other part of the convective line is embedded in significant stratiform precipitation.

Meanwhile, nonlinear MCSs are categorized into three distinct groups objectively, namely, near-circular MCSs (NC), broad stratiform MCSs (BS), and other MCSs (OT). First, nonlinear MCSs with a ratio of shorter to the longer dimension of the convective region > 0.6 are classified as NCs (Liu and Zipser 2013a). Liu and Zipser (2013a) reported that the convective intensity of near-circulative systems (over the entire tropics/subtropics) is stronger than the linear convective systems, whose conclusion was somehow contradictory to the traditional concept that linear convective systems (squall lines) are more likely to produce severe weather. Therefore, it is intriguing whether this conclusion also applies to MCSs in China. Second, nonlinear MCSs containing an extremely large area of stratiform precipitation ($> 40000 \text{ km}^2$) are identified as BSs following Houze et al. (2015). Finally, nonlinear MCSs that are not categorized as NCs or BSs are assigned as OTs.

c. MCS statistics

All MCSs are numbered after being identified, and grid cells (0.05°) within the same MCS are tagged by the corresponding MCS number. The climatological MCS probability (section 3) is calculated as the number of MCS grid cells (0.05°) within a $1^\circ \times 1^\circ$ box divided by the total number of grid cells (0.05°) sampled by PR and DPR in the same box. Similarly, the climatological rainfall contribution (section 3) from MCSs is computed as the summation of MCS precipitation divided by the total precipitation over a $1^\circ \times 1^\circ$ grid box.

MCS centroids (elliptical fitting) are assigned as the MCS centers along with time and location information.

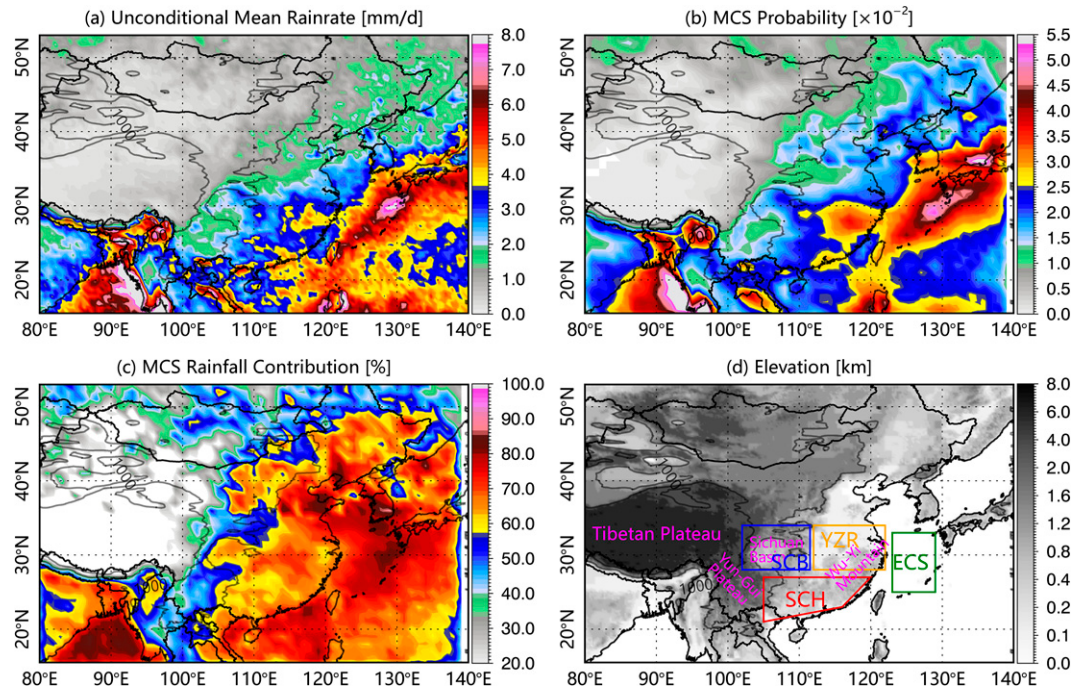


FIG. 1. Distribution of (a) annual mean rain rate (unconditional, mm day^{-1}); (b) MCS frequency, defined by probability (10^{-2}) over $1^\circ \times 1^\circ$ grids; (c) annual rainfall contribution (%) from MCSs; and (d) terrain elevation height (km). In (d), the yellow, red, green, and blue rectangles indicate the Southern China (SCH), Yangtze River valley (YZR), Eastern China Sea (ECS), and Sichuan (SCB) regions, respectively, and the magenta text indicates the topographical features. The black contours in all panels represent elevations of 1000 and 3000 m.

Distributions of MCSs in section 4 and section 5 are based on MCS centers, for consistency to previous squall lines studies. A variety of TRMM/GPM parameters are saved as proxies for MCS's precipitation intensity, horizontal structure, convective intensity, and microphysical property (analyzed in sections 4 and 5). These variables include MCS's precipitation area, maximum rain rate, the volume of heavy precipitation ($>10 \text{ mm h}^{-1}$), the areal fraction of stratiform-type rain, total lightning flash rate, maximum echo-top heights of 20 dBZ (Maxht20) and 35 dBZ (Maxht35), and minimum microwave brightness temperature (polarization corrected temperature, PCT) at 85 GHz (Min85PCT) and 37 GHz (Min37PCT).

d. Reanalysis data

The European Centre for Medium-Range Weather Forecasts fifth-generation reanalysis data (ERA5) (Hersbach et al. 2020) are used to investigate the large-scale environmental conditions for MCSs of various organizational modes. We utilize the ERA5 data at a 0.25° horizontal resolution and 3-hourly temporal resolution with 11 vertical levels. Environmental conditions 3 h prior to MCSs occurrence are composited as a function of MCS organizational modes. Specifically, ERA5 fields of winds, relative humidity, geopotential height, and divergence at the lower (850-hPa), middle (500-hPa), and upper (200-hPa) levels are analyzed. The convective available potential energy (CAPE) and convective

inhibited energy (CIN) are derived from the ERA5 temperature and dewpoint profiles (11 levels).

3. Spatiotemporal variations of MCSs over China

This section first provides a broad picture of MCSs over the broad East Asia region, and then examines more detailed characteristics of MCSs over China. MCS climatology over the entirety of East Asia ($15^\circ\text{--}55^\circ\text{N}$, $80^\circ\text{--}140^\circ\text{E}$) is derived through combining TRMM and GPM observations (section 3a). A total of 48 804 and 14 757 MCSs are identified over East Asia from TRMM and GPM, respectively. It should be noted that the MCS frequency may be overestimated (Schumacher and Rasmussen 2020), as the MCS life duration is not counted here (PR and DPR are not capable to provide high temporal resolution data). The GPM-based MCS samples in the middle and higher latitudes (north of 38°N) are relatively small. Therefore, seasonal and diurnal variations of MCSs (sections 3b–3c) are only examined using TRMM data over the MCS-populated region in China ($15^\circ\text{--}35^\circ\text{N}$, $100^\circ\text{--}140^\circ\text{E}$), considering the ample sample and long-term consistency of TRMM.

a. Geographical distribution and rainfall contribution

Distributions of annual rainfall, MCS population, and rainfall contribution by MCSs over East Asia are presented in Figs. 1a–c, with elevation information provided in Fig. 1d. Generally, East Asia is featured by an offshore heavy rainband

(5–6 mm day⁻¹) ranging from South China Sea (SCS) to southern Japan, and a precipitation pattern decreasing stepwise from eastern China (3–4 mm day⁻¹) to the foothills (1.5–2 mm day⁻¹) of the eastern Tibetan Plateau. Annual rainfall also decreases from the central to northern China due to the reducing influence of the summer monsoon. The greatest accumulated rainfall in mainland China occurs over the Wu-Yi Mountain areas (marked in Fig. 1d) in southeast China, possibly due to the elevated frequency of mei-yu fronts over that region (Ding and Chan 2005; Xu et al. 2009) in combination with orographic enhancement. Another rainfall maximum appears in the coastal southern China (SCH; marked in Fig. 1d). These radar-based rainfall patterns are consistent with precipitation climatology from multisatellite rainfall products (Xu 2020) and rain gauge measurements (Zhou et al. 2008). Moreover, the radar-estimated precipitation over coastal regions and steep terrain displays a stronger gradient compared to rainfall derived from passive microwave/IR or rain gauge (Xu 2020; Zhou et al. 2008).

The spatial distribution of MCS frequency (probability, Fig. 1b) in East Asia largely mimics that of precipitation (Fig. 1a). MCSs contribute over 50%–60% of the total rainfall over regions influenced by the summer monsoon, and less than 20%–30% over arid areas such as the Tibetan Plateau and northwest China (Fig. 1c). Similarly, MCSs contribute more than 50% of the warm season rainfall in most regions to east of the Rocky Mountains in the United States (Fritsch et al. 1986; Ashley et al. 2003; Feng et al. 2016; Haberlie and Ashley 2019; Feng et al. 2019). It should be noted that the rainfall fraction due to MCSs in this study may be overestimated by polar-orbiting satellites (TRMM/GPM) as many deep convective storms may not meet the MCS life-duration threshold but easily satisfy the dimensional criteria (Wang et al. 2019; Schumacher and Rasmussen 2020). Over China, an obvious MCS band (Fig. 1b) shows up from the Sichuan basin to the lower reaches of the Yangtze River (YZR) and Wu-Yi Mountain areas (geographics marked in Fig. 1d). Maximum MCS activity also occurs over SCH to the east of the Yun-Gui Plateau. Interestingly, MCSs frequently develop over Northeast China (Fig. 1b), where the annual rainfall amount is relatively limited (Fig. 1a). These MCS climatologies are generally consistent with results based on IR observations and multisatellite rainfall products (Zheng et al. 2008; Yang et al. 2015; Feng et al. 2021). A significant number of MCSs develop over the second-step terrain just east of the eastern Tibetan Plateau, which frequently propagate eastward and contribute a large fraction of rainfall over the lower reaches of the YZR (Yang et al. 2018). However, there is little MCS activity over the Plateau (Fig. 1b), contrasting to the maximum MCS band over the southern Plateau reported in IR-based studies (Zheng et al. 2008; Yang et al. 2015; Chen et al. 2019; Mai et al. 2021). This suggests that convective cloud systems over the plateau may have extensive and very thick, cold cloud shields (revealed by IR measurements) but minimum precipitation down to the ground (not detectable by the spaceborne radars). This is likely because that the air below these cold clouds is dry over

the Plateau, so not much moisture is available to produce rainfall.

b. Seasonal variability

The monthly mean MCS frequency is shown for the warm season with the 850-hPa winds in Fig. 2. Seasonal variations of MCS frequency in East Asia are closely related to the progression and retreat of the summer monsoon (Wang 2006; Ding and Chan 2005; Ding 2007). Before the onset of the summer monsoon over the SCS (April), MCSs already actively develop over central eastern China to the east of the Sichuan basin (Fig. 2a), possibly due to frequent cold front activity (Xu et al. 2009; Lin et al. 2021). Maximum MCS activities during the spring season are also reported over the CONUS due to the increase of surface heating and enhanced low-level southwesterly/southerly flows in the spring (Haberlie and Ashley 2019; Feng et al. 2019). After the onset of the SCS monsoon (strong southwesterlies) in May–June, maximum MCS frequency occurs over the SCH (southernmost China), as the warm and moist monsoon flows impinge on the coast and coastal mountains (Xu et al. 2009; Xu and Zipser 2011; Ding and Chan 2005). The MCS frequency maxima coincide with the convergence of the low-level flows. Both MCSs and the low-level southwesterlies migrate northward from May to July along with the monsoon progression (Wang 2006; Ding and Chan 2005; Ding 2007). In June, MCSs penetrate farther westward, up to the foothills of the Tibetan Plateau or the Yun-Gui Plateau, likely due to a warmer and moister environment with the full establishment of the summer monsoon in China. MCS maxima are located farther north in August (not shown). In September, MCSs over the entire mainland China decrease rapidly with the retreat of the summer monsoon, as indicated by the switch of southwesterly/southerly low-level winds to easterly/northeasterly flows. These MCS seasonal patterns are generally close to previous MCS climatologies based on rain gauge-satellite combined precipitation data and the IR observations (Li et al. 2020; Yang et al. 2015). However, the radar-observed MCS distribution in this study shows a more evident band-shaped feature (e.g., compared to Fig. 3 in Zheng et al. 2008 and Fig. 6 in Yang et al. 2015) associated with the mei-yu front and stronger seasonal migration patterns, realistically representing the mei-yu rainband and its northward progression (Ding and Chan 2005; Ding 2007).

c. Diurnal variations

Besides seasonal variability, MCS also exhibits strong diurnal variations (Fig. 3). MCS frequency over the YZR and SCH peaks in the early morning and afternoon, respectively. MCSs over Sichuan Basin and the key mei-yu rain belt (from middle reaches of the YZR to Japan) start to increase at midnight (0000–0300 LT) and maximize in the early morning (0300–0900 LT). This nocturnal MCS peak is evident over both land and ocean within the mei-yu rain belt. The morning enhancement of MCS frequency over the YZR is consistent with the nocturnal rainfall peak previously reported, which is related to the strengthening of the southwesterly low-level jet

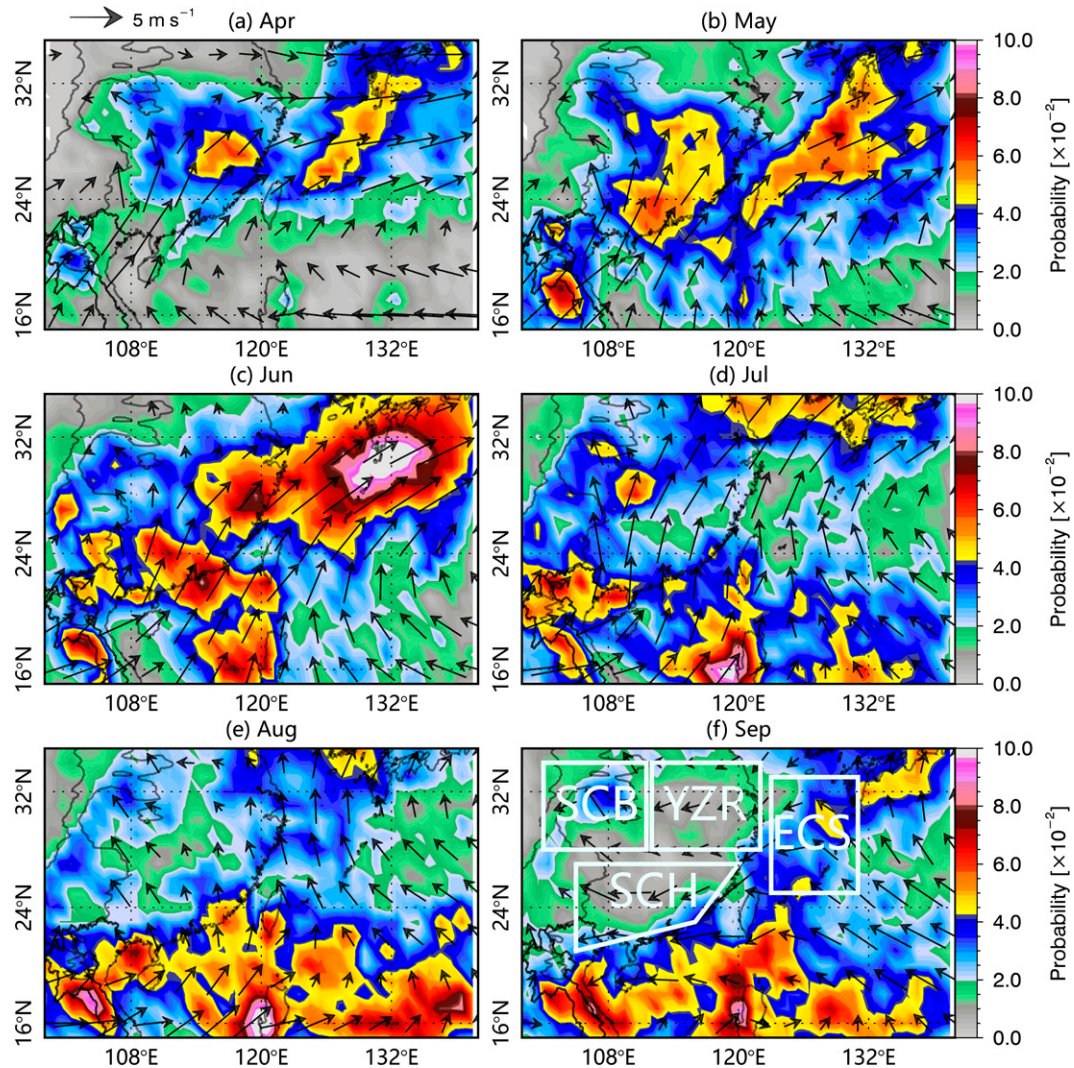


FIG. 2. Geographical distributions of monthly mean (April–September) MCS frequency (probability) from 1998 to 2014 using only TRMM PR observations overlaid with monthly mean winds at 850 hPa (vectors) derived from ERA5 data.

from SCH and the enhancing moisture convergence in the YZR mei-yu rainband (Geng and Yamada 2007; Cui et al. 2020; Guan et al. 2020). Over the CONUS, summertime MCSs frequently initiate on the lee side of the Rocky Mountains and propagate eastward into the Great Plains in the nocturnal hours (Carbone and Tuttle 2008; Zhang et al. 2014; Feng et al. 2019). However, this study shows no significant eastward propagation signal on MCSs developed over the foothills of the eastern Tibetan Plateau including the Sichuan basin. This is possibly because the MCS frequency over the downstream (YZR) is enhanced by the nocturnal convergence (Cui et al. 2020; Guan et al. 2020) in the mean time when MCSs developed over the foothill regions due to mountains–plains soleiloids (Xu and Zipser 2011; Bao et al. 2011). On the other hand, MCSs over SCH evolve more like typical continental convection, which peak in frequency in the afternoon and diminishes in the morning.

The diurnal cycle of MCS properties over several selected regions are further examined (Fig. 4). The diurnal patterns of MCS number (storm-scale, Fig. 4a) are generally consistent with the gridscale MCS frequency (Fig. 3). There are two peaks of the MCS number over YZR (red curves), a primary one in the early morning and a secondary one in the afternoon (Fig. 4a). However, MCS rain area and precipitation intensity over YZR are the most enhanced in the early morning and minimized in the afternoon (Figs. 5b,c). Though the MCS population over the SCH (black curves) maximizes in the afternoon, their size and precipitation intensity markedly peak in the early morning, possibly due to MCS upscale growth and/or precipitation enhancement by the nocturnally strengthened low-level jet over SCH (Du et al. 2020). The number, rain area, and rain rate of MCSs over Sichuan Basin (blue curves) all peak in the early morning when lower-level convergence over the Basin becomes the most

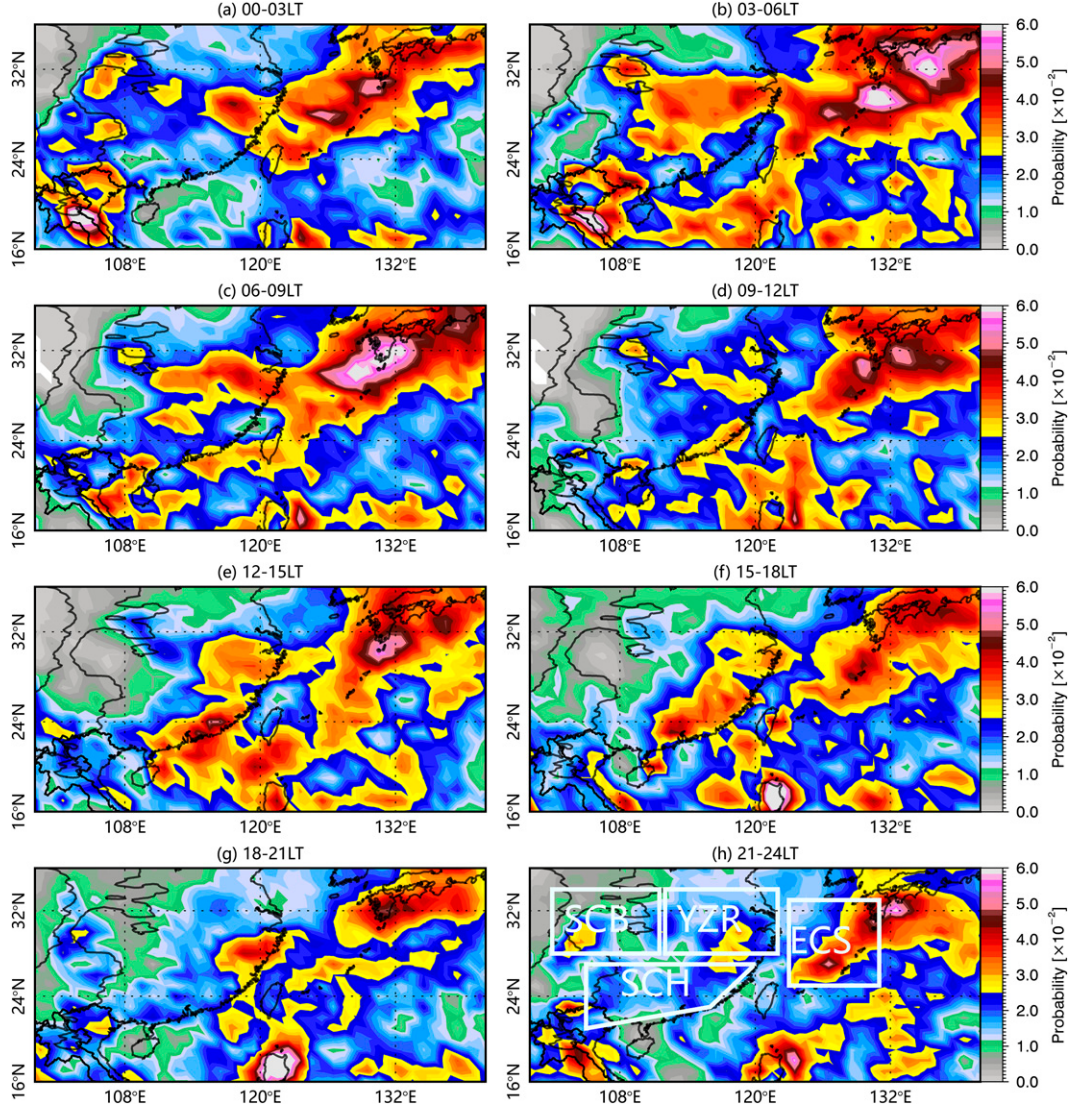


FIG. 3. Diurnal variations of PR-based MCS frequency (probability) composited in local time: (a) 0000–0300, (b) 0300–0600, (c) 0600–0900, (d) 0900–1200, (e) 1200–1500, (f) 1500–1800, (g) 1800–2100, and (h) 2100–2400 LT.

enhanced (Xu and Zipser 2011; Bao et al. 2011). Over the oceans (green curves), the population and rain rate of MCSs are elevated in the morning, while their rain areas show little diurnal variability.

4. Comparisons between linear and nonlinear MCSs

Though the total MCSs and linear MCSs in China have been investigated by many studies, their differences (especially convective intensity) are still less known. Therefore, this section compares characteristics of linear (LN) versus nonlinear MCSs over land areas of China (20° – 35° N, 96° – 121° E). A total of 10 173 MCSs are identified in this region from TRMM PR observations (Table 1), ~600 MCSs per year. Li et al. (2020) tracked the long-lived (> 6 h) MCSs over a similar region in eastern China (21° – 38° N, 102.5° – 121.5° E) using hourly gauge-

satellite-combined rainfall product and found an annual mean MCS frequency of 420 yr^{-1} . Given that a significant fraction of MCSs do not last 6 h, MCS frequency in this study is comparable to that reported by Li et al. (2020). Nearly 20% of the MCSs are linearly organized, while more than 80% MCSs are nonlinear. Only 13% and 8% of the MCSs are identified as near-circular (NC) and broad stratiform (BS) systems, respectively, and 61% of the MCSs are categorized as other types (OT). In other words, fractions of linear MCSs in China are lower than those in the CONUS (23%–40%) reported by studies using ground-based radar observations (Gallus et al. 2008; Ashley et al. 2019; Cui et al. 2021). This difference is possibly because the environment conditions of continental United States are more conducive to linear MCS organization such as stronger vertical wind shear (Meng et al. 2013).

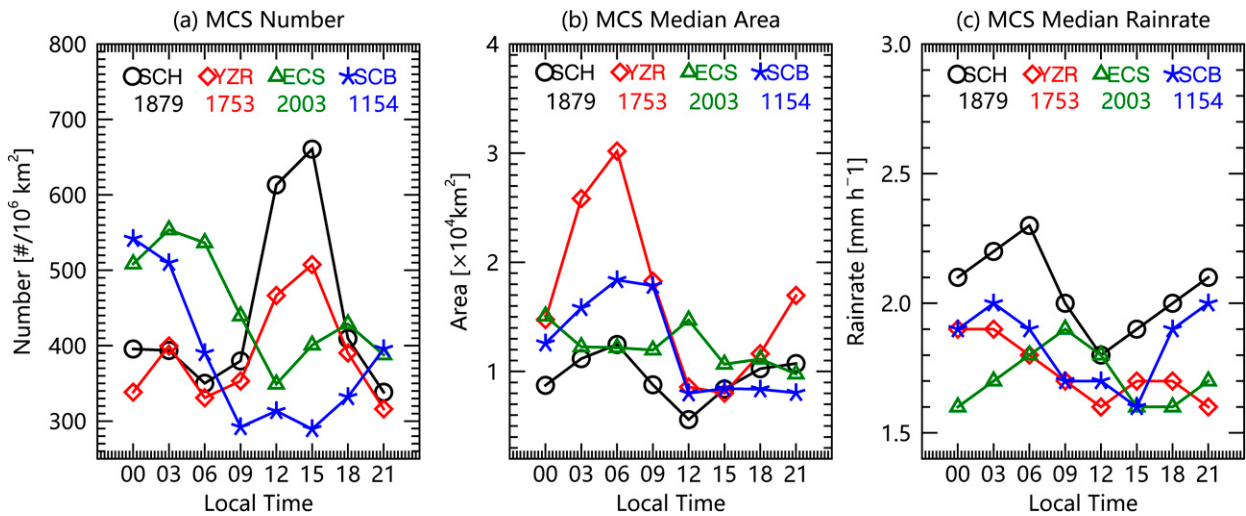


FIG. 4. Time series (3-hourly local time) of (a) number of MCSs, (b) MCS median area, and (c) MCS median rain rate over the various regions including SCH (black), YZR (red), ECS (green), and SCB (blue) marked in Fig. 1b.

a. Geographical distribution and large-scale conditions

The locations and rainfall contribution of MCSs in various categories (LN versus nonlinear systems) are presented in Fig. 5. LNs mainly occur over lower-elevation regions (<1000 m) in the eastern and southern China (Fig. 5a), consistent with maximum squall lines over the Great Plains in CONUS (Ashley et al. 2019; Cui et al. 2021). LNs contribute 20%–25% of the total rainfall over these regions (Fig. 5b). These results are generally consistent with the squall-line frequency reported by ground-based radar studies (Meng et al. 2013; Zheng et al. 2013), e.g., over the Jiangsu province. However, MCSs are also quite frequent over Wu-Yi Mountain, which was not detected by the ground-based radars (Meng et al. 2013). Meng et al. (2013) pointed out that ground-based radars may be subjected to significant beam blockage (missing data) in hilly areas like Wu-Yi Mountain. On the other hand, NCs distribute more evenly over the lower-rising (<1000 m) areas in China and have a limited contribution to the regional rainfall (5%–10%). BSs show a maximum frequency band ranging from the central (Sichuan basin) to eastern China (Wu-Yi Mountain) and contribute 15%–20% of the total rainfall in these regions (Figs. 5e,f). Compared to the LN and BS, OTs penetrate farther west and show a maximum along the Yun-Gui plateau and foothills of the eastern Tibetan Plateau (>1000 m), where OTs contribute more than 30% of the annual rainfall (Figs. 5g,h).

To better understand the large-scale conditions responsible for each MCS category, their environmental variables are composited (anomalies with respect to the climatology), respectively (Fig. 6). In these composites, seasonal (April–August) means are subtracted from averages during times when a given MCS category is present over the key region, where most of these MCSs occurred (marked by the white box). In general, the large-scale circulations and thermodynamic conditions of MCSs are all enhanced and share certain similarities among various categories. The large-scale features of MCSs

(compared to the seasonal mean) include strengthened low-level (850 hPa) southwesterly winds, moister environments at both the lower and middle (500 hPa) levels, and stronger upper-level (200 hPa) divergence. However, there are also significant differences in the environmental conditions among the four MCS categories. LNs are associated with the most enhanced low-level flows, deep midlevel troughing, and the strongest upper-level westerly jets, as well as the greatest upper-level divergence. BSs show a similar large-scale condition as LNs but an even moister midtroposphere and deeper midlevel trough, possibly because some LNs eventually evolve into BSs under a moist midlevel and stronger troughing dynamic conditions. Compared to LNs and BSs, NCs and OTs are associated with a relatively weaker dynamical (no troughing) and thermodynamical (drier) environment.

b. Precipitation characteristics and convective properties

The convective intensities and structure may determine the type and severity of MCS impacts (e.g., flooding and hail), therefore, their differences between LNs and nonlinear MCSs in China are further examined here. Note that only warm-season MCSs (80%) are considered for analyses, as cold-season MCSs (20%) have generally weak convection. The cumulative distribution frequency (CDF) of LNs and nonlinear MCSs are calculated as a function of rain area, areal fraction of stratiform rain, maximum rain rate, and heavy rain ($>10 \text{ mm h}^{-1}$) volume (Fig. 7). First of all, LNs (median of $\sim 1.5 \times 10^4 \text{ km}^2$) are generally larger than nonlinear MCSs ($\sim 1 \times 10^4 \text{ km}^2$) except BS (Fig. 7a). BSs own the largest rain areas and the greatest fraction of stratiform precipitation (Figs. 7a,b), likely because they have the strongest wind shear and greatest amount of midlevel moisture (Table 1). LNs and nonlinear MCSs (except BS) share a similar stratiform rain fraction CDF with a median value of around 70%. Furthermore, LNs frequently produce extremely high peak rain rates (median of 70 mm h^{-1}), much more intense than nonlinear MCSs (Fig. 7c). Interestingly, BSs

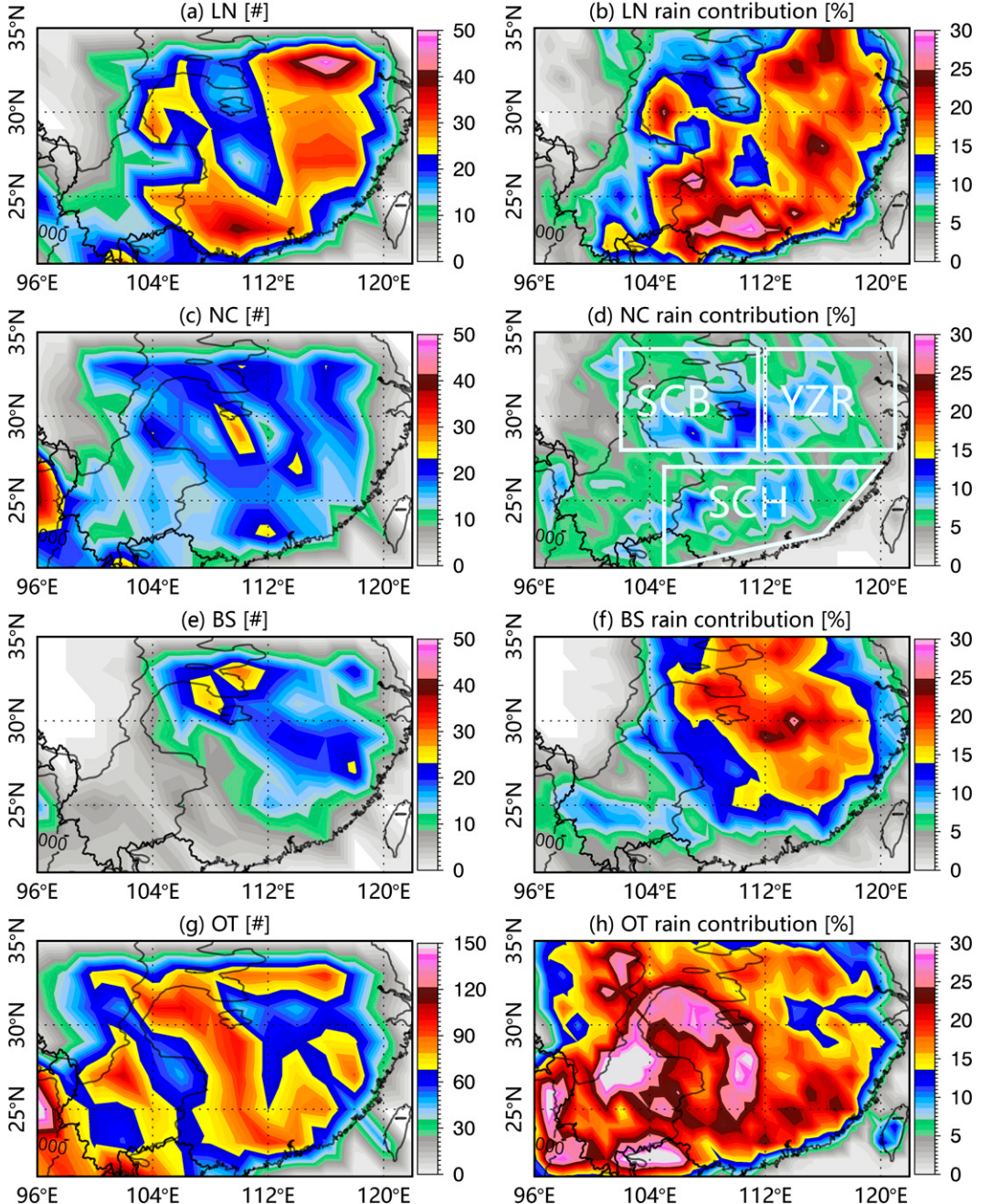


FIG. 5. (left) Number and (right) annual rainfall contribution (%) of MCSs in different categories: (a),(b) LN; (c),(d) NC; (e),(f) BS; and (g),(h) OT. MCS number and rainfall fractions are calculated over a $2^\circ \times 2^\circ$ grid box.

(dominated by broad stratiform rain) have a greater peak rain rate than other nonlinear MCSs. BSs also generate very large heavy precipitation ($>10 \text{ mm h}^{-1}$) volumes (amounts), similar as the LNs (Fig. 7d). This indicates the great potential of both BSs and LNs in inducing heavy rain events. In contrast, NC and OT systems own much smaller heavy rain volumes.

Convective intensities of MCSs are examined in terms of CDFs of TRMM convective parameters, including Maxht20, Min85pct, Maxht35, and lightning flash rate (Fig. 8). These TRMM proxies

all indicate that LNs have the strongest convection and BSs the weakest. Nearly 60% LNs have precipitation-sized particles (20 dBZ) reaching above 12 km (Fig. 8a), a well-accepted deep convective threshold (Liu et al. 2008; Xu and Zipser 2012; Xu 2013). Also, more than 20% of the LNs may induce overshooting, i.e., the echo-top height of $20 \text{ dBZ} > 16 \text{ km}$, an altitude that is very possibly above the tropopause in east Asia (Xu 2013; Liu and Liu 2016). Furthermore, the depressed microwave PCT (85 GHz) signature of

TABLE 1. Samples and environmental conditions of MCSs in various categories including linear MCS (LN), near-circular MCS (NC), broad-stratiform MCS (BS), and other MCS (OT) over the selected region (20° – 35° N, 96° – 121° E) in China based on TRMM PR data from 1998 to 2014.

	All MCS	LN	NC	BS	OT	Nonlinear MCS
Population (fraction)	10173	1733 (17.0%)	1407 (13.8%)	827 (8.1%)	6206 (61.0%)	
Wind shear of 200–850 hPa ($m s^{-1}$)	19.4	20.4	18.6	26.1	18.6	
Relative humidity at 500 hPa (%)	67.1	63.3	66.75	73.4	67.4	

LNs (a median value of \sim 150 K) suggests the presence of a very deep column of ice particles in these storms (Fig. 8b). Similarly, the majority of LNs (>50%) have graupel-sized particles (35 dBZ) in the deep mixed-phase region (Fig. 8c), i.e., 8–9 km (equivalent to -15° to -20° C). Most LNs (70%) have at least one lightning flash observed by the TRMM LIS (Fig. 8d), and 30%–40% LNs are associated with intense thunderstorms, e.g., a flash rate of 10–20 flashes per minute (hereinafter abbreviated $fl min^{-1}$) (Cecil et al. 2005; Zipser et al. 2006).

BSs show the weakest convective intensities, for instance, only 10% BSs satisfy the abovementioned intense convection thresholds (i.e., $Maxht35 > 8$ km or $fl min^{-1} > 10$). The population-dominant OTs show only weak-to-moderate mixed-phase process (median $Maxht20 \sim 6$ km), even though their convective depth ($Maxht20$) and total ice water path (PCT85) are quite impressive. On the other hand, the convective intensities of the NCs are in between the LNs and BSs. Liu and Zipser (2013a) reported that NCs have stronger convection than LNs. However, their objective MCS

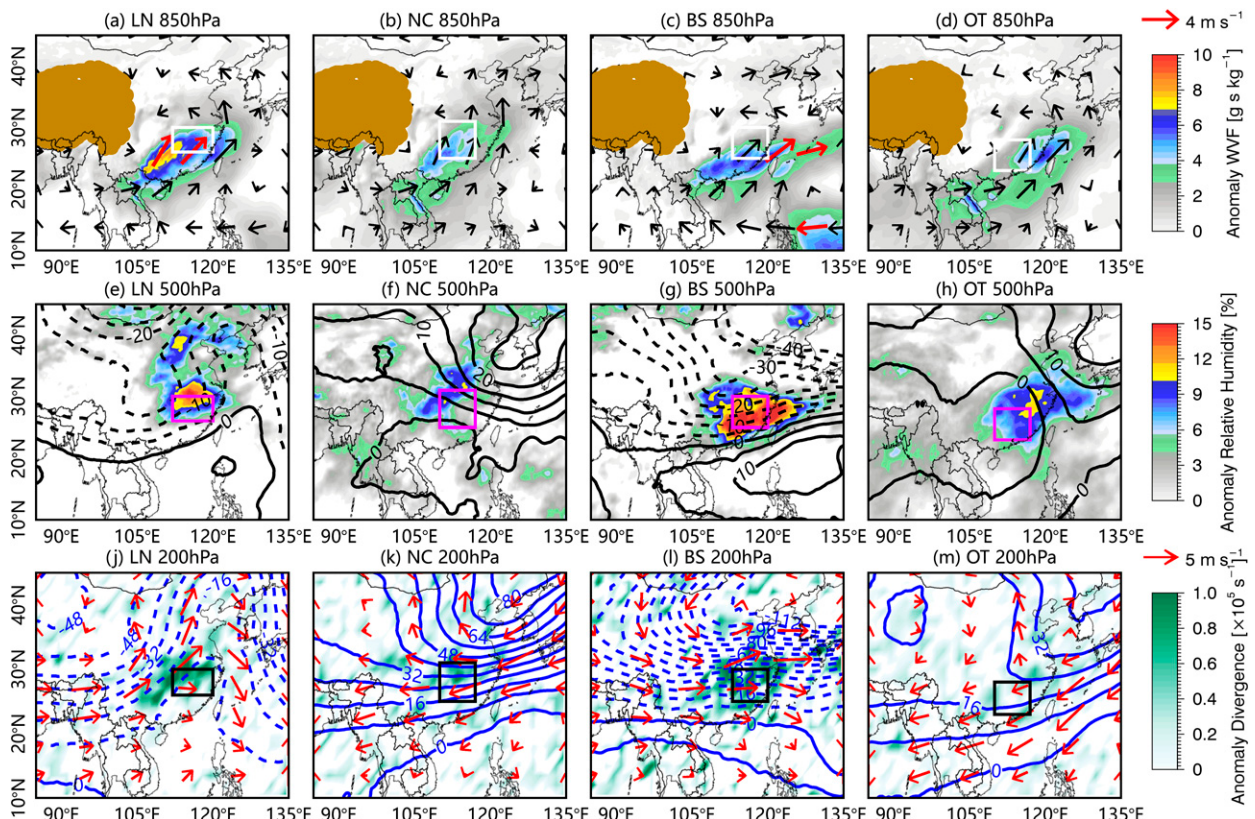


FIG. 6. Composited large-scale environments (all anomalies) of MCSs in different categories during April–August: (a)–(d) 850-hPa wind and water vapor flux (color shaded); (e)–(h) 500-hPa geopotential height and relative humidity (color shaded); and (j)–(m) 200-hPa wind, geopotential height, and divergence (color shaded). The rectangle (black or white) marks the highest-frequency region of MCS in specific category selected for analysis. In (a)–(d), red wind vector represents a wind speed greater than $5 m s^{-1}$. In (a)–(d), data are blanked out over the 3500-m elevation (golden color filled). The anomalies are the differences between the four MCS modes and the seasonal mean conditions (MCS minus seasonal mean).

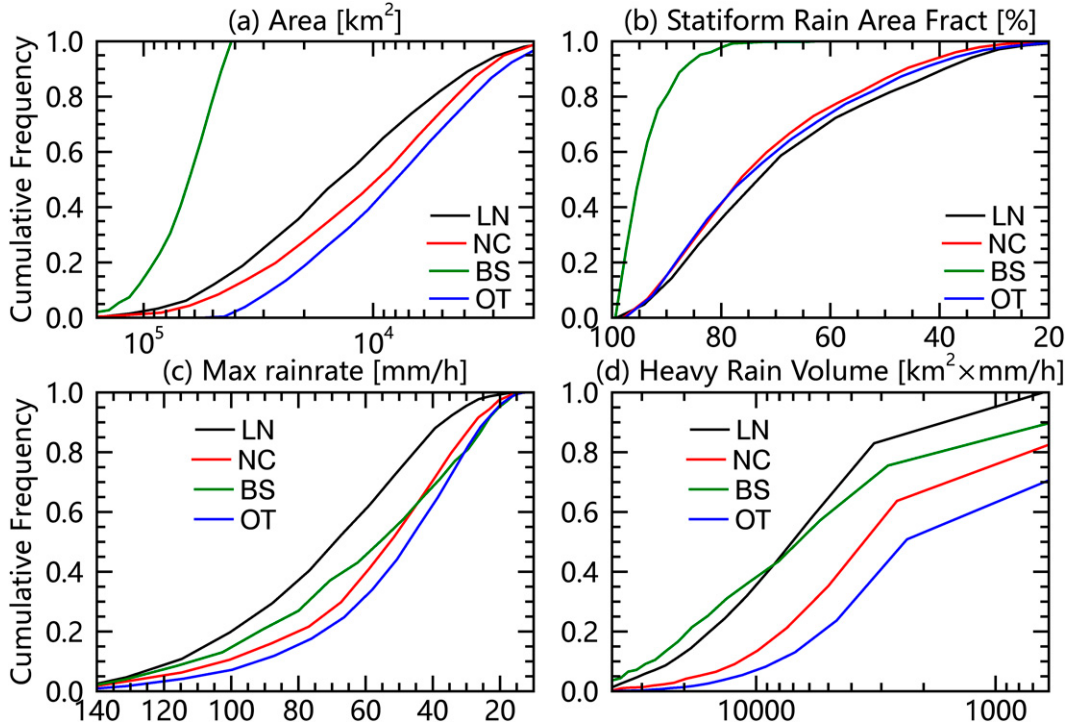


FIG. 7. Cumulative distribution frequency of MCSs over land for 20° – 35° N, 90° – 125° E during April–August as a function of: (a) precipitation area, (b) stratiform rain area fraction, (c) maximum rain rate, and (d) heavy rain ($>10 \text{ mm h}^{-1}$) volume. Different colors represent various MCS categories.

classification technique likely includes some intense BE (linear) convection in the NC category (Liu and Zipser 2013a).

5. Squall lines in various organizational modes

Previous sections have examined the spatiotemporal variations of MCSs in China and found significant differences between linear and nonlinear MCSs. This section further emphasizes the structural difference among linear MCSs in various organizational modes, including TS/LS, BE, EL, NS, and PS. Of the 1733 linear MCSs identified in the study region (Table 2), TS/LS systems have the highest frequency (46.2%), followed by NS (28.3%), PS (10.5%), BE (8.7%), and EL (6.4%). These relative frequencies among various linear MCS organizational modes are consistent with previous results using ground-based radar data either in eastern China or the CONUS (Parker and Johnson 2000; Gallus et al. 2008; Zheng et al. 2013; Ma et al. 2021).

a. Locations and storm environments

Geographic distributions of various types of linear MCSs are shown in Fig. 9. The most populated TS/LS storms widely distribute over the lower-rising areas ($<1000 \text{ m}$) with a maximum center located over the east/southeast China (Fig. 9a). There are also a significant number of TS/LS systems situated over the Yun-Gui Plateau (1000–2000 m) in the southwest China. BEs mainly occur over eastern China (Jiangsu Province and Wu-Yi Mountain) and southernmost China near the

Yun-Gui Plateau (Fig. 9b). EL systems are the most populated over Wu-Yi Mountain and Sichuan Basin (Fig. 9c), likely due to orographic enhancement in these areas. Also, EL MCSs (Fig. 9c) mainly occur to the north of $\sim 25^{\circ}$ N, possibly due to reduced wind shear over the southernmost China (Xu 2013; Xu 2020). Zheng et al. (2013) showed that EL systems are dominant over the central east China during summer, as most convective lines over there are embedded in large-scale stratiform precipitation along the mei-yu front. Maxima in the occurrence frequencies of both NS and PS storms occur the eastern plains to the north of the YZR and the southeast edge of the Yun-Gui Plateau.

The large-scale environments among various organizational modes of squall lines are generally similar, but with some distinguishable features. Figure 10 shows the anomalies of large-scale conditions during times when a given MCS category is present over the key region (marked by the white box) relative to the climatological mean. TS has enhanced low-level southwesterly winds, the most elevated moisture flux at 850 hPa (Fig. 10a) and a moderate CAPE ($\sim 1000 \text{ J kg}^{-1}$, Table 2). Cui et al. (2021) also reported similar storm environments for TS systems in the CONUS. In addition to the enhanced low-level flows ($\sim 8 \text{ m s}^{-1}$), BE is associated with the deepest midlevel (500 hPa) troughing (Fig. 10g), the largest CAPE ($\sim 1300 \text{ J kg}^{-1}$), and the strongest CIN (Table 2). EL, the largest linear MCS (will be shown later), is characterized by an enhanced trough and the moistest middle level (Fig. 10h), as well as the strongest

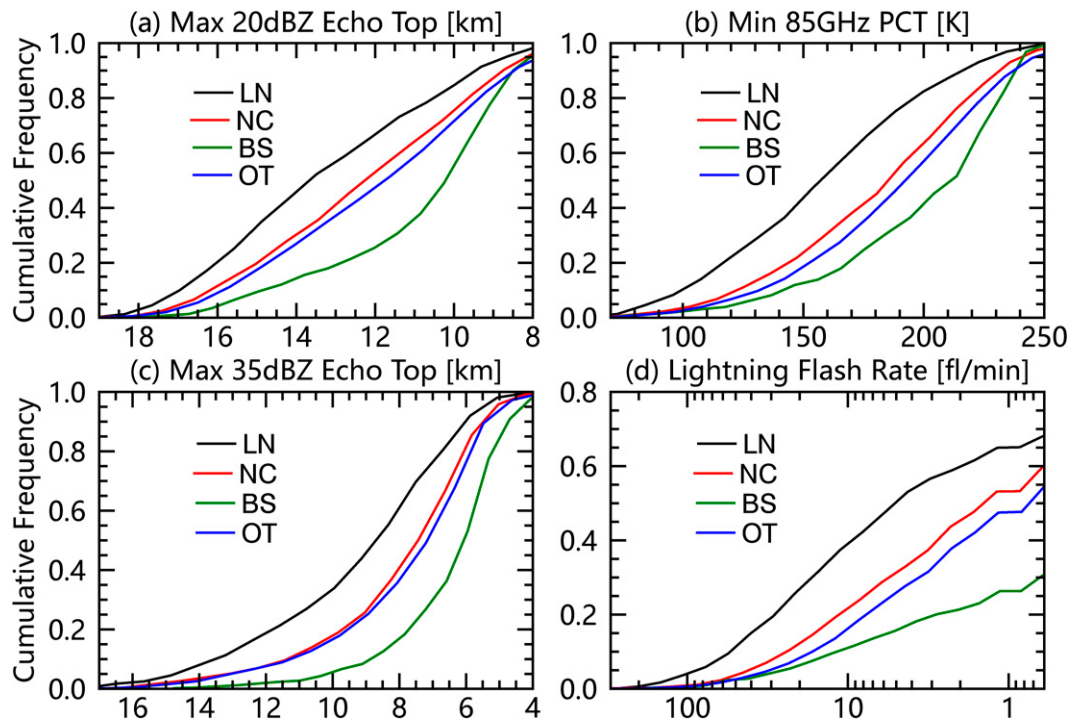


FIG. 8. As in Fig. 7, but for different variables: (a) maximum height of 20-dBZ echo, (b) minimum PCT at 85 GHz, (c) maximum height of 35-dBZ echo, and (d) lightning flash rate.

vertical wind shear (Table 2) likely associated with mei-yu front (Zheng et al. 2013). PS occurs under conditions with relatively shallower midlevel trough and weakest upper-level jets. Overall, TS/LS, BE, EL, and PS mostly occur ahead of a midtropospheric trough and are associated with upper-level divergence, which are similar to situations in the CONUS (Cui et al. 2021). On the other hand, NS exhibits the weakest large-scale dynamics, e.g., weakest low-level winds, little (if any) midlevel trough, lowest wind shear, and the largest displacement from the upper-level jet stream. Therefore, NS is more like thermally driven convection under moderate CAPE ($\sim 930 \text{ J kg}^{-1}$, Table 2).

b. Precipitation characteristics and convective properties

Besides the distributions and environments of specific linear MCS categories, their precipitation characteristics and convective structure are also important to know. The CDFs of precipitation area, stratiform rain fraction, maximum rain rate, and volume of heavy precipitation in linear MCSs are

shown in Fig. 11. EL owns the largest rain area and the highest areal fraction of stratiform precipitation, while NS has the smallest (Figs. 11a,b). Nearly half of the EL systems satisfy the areal threshold of BSs ($>40\,000 \text{ km}^2$), whereas the median NS storms only have a rain area of $\sim 5000 \text{ km}^2$. These characteristics are associated with the moistest midtroposphere and the largest wind shear of ELs, and the much drier midlevel and reduced shear of NSs (Table 2). TS/LS, PS and BE systems are also quite extended, with a median rain area of $\sim 20\,000 \text{ km}^2$. Note the actual precipitation areas of all the systems should be larger than what have been shown here, as the sensitivity of TMM PR is $\sim 18 \text{ dBZ}$, equivalent to a rain rate of 0.5 mm h^{-1} . In addition, EL systems have an extremely high stratiform rain fraction ($\sim 95\%$), close to BSs (Fig. 7). Of all the linear MCSs, BE produces the heaviest peak rain rate (median of $\sim 80 \text{ mm h}^{-1}$) and the greatest heavy-rain volume (Figs. 11c,d).

Different types of linear MCSs also show different convective intensities and ensemble microphysics (Fig. 12). In

TABLE 2. Samples and environmental conditions of linear MCSs in various organizational modes, including trailing stratiform and leading stratiform (TS/LS), bow echo (BE), embedded line (EL), no stratiform (NS), and parallel stratiform (PS).

	TS/LS	BE	EL	NS	PS
Population (fraction)	802 (46.2%)	150 (8.7%)	110 (6.4%)	489 (28.2%)	182 (10.5%)
Wind shear of 200–850 hPa (m s^{-1})	21.3	15.1	24.6	16.8	23.1
Relative humidity at 500 hPa (%)	69.0	65.2	83.0	58.1	69.3
CAPE (J kg^{-1})	967	1297	805	930	754
CIN (J kg^{-1})	47	60	40	51	40

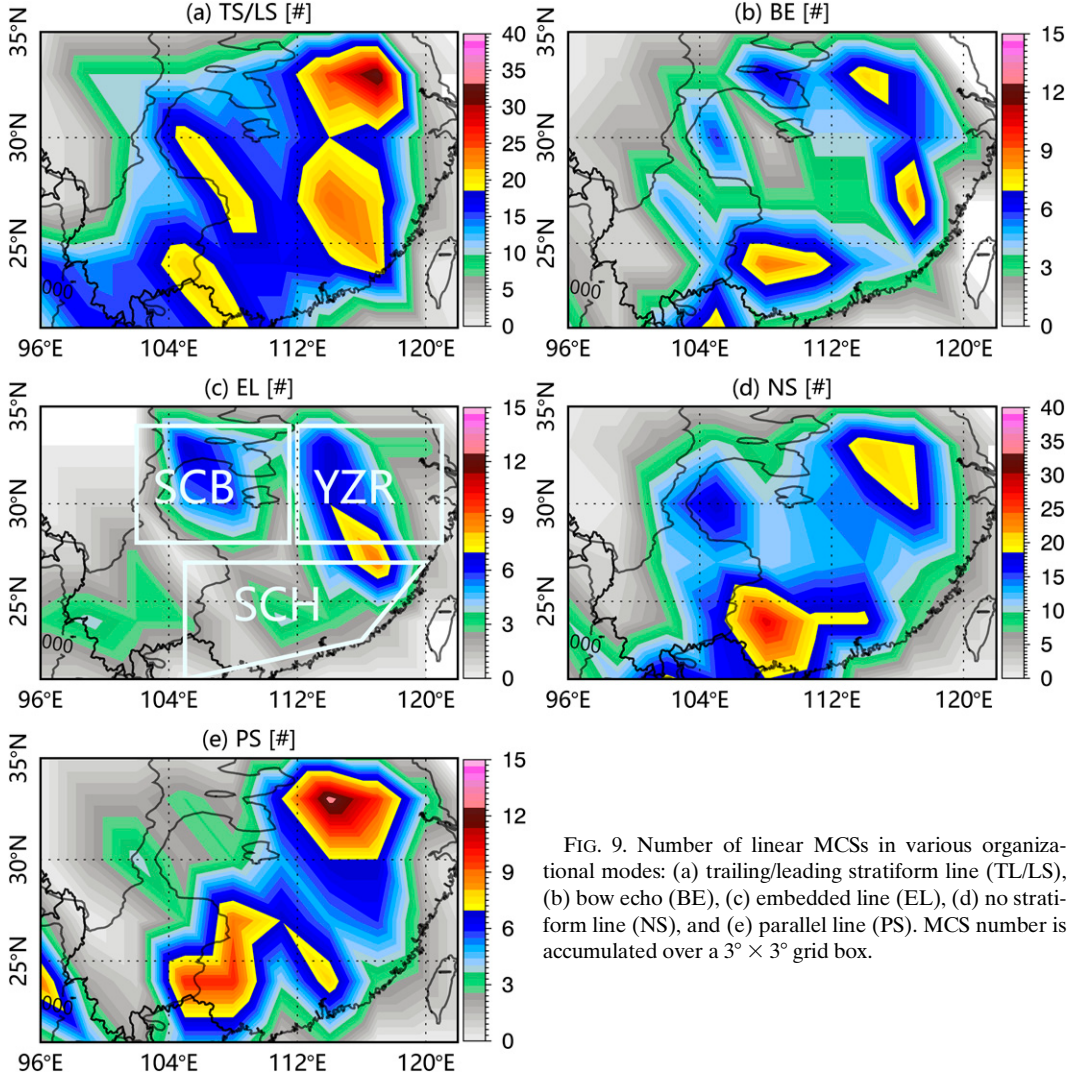


FIG. 9. Number of linear MCSs in various organizational modes: (a) trailing/leading stratiform line (TL/LS), (b) bow echo (BE), (c) embedded line (EL), (d) no stratiform line (NS), and (e) parallel line (PS). MCS number is accumulated over a $3^\circ \times 3^\circ$ grid box.

addition to precipitation intensity (Fig. 11c), BE also shows the strongest convective intensities indicated by various TRMM proxies (Fig. 12). The broad EL systems exhibit the weakest convective intensity, and other linear MCSs (NS, TS/LS, and PS) have relatively strong convection. Specifically, nearly 50% (30%–40%) of the BE (NS, TS/LS, and PS) storms have 20-dBZ echo tops (Maxht20) extended near or above the tropopause (15–16 km). The median Maxht20 of BE is significantly higher (1–2 km) than TS/PS/NS, and much taller (4 km) than that of EL (Fig. 12a). BE also shows very cold microwave brightness temperature at 85 GHz (Min85pct), with a median value of 145 K (Fig. 12b). The second group of the linear MCSs (NS, TS/LS, and PS) still induce impressive ice scattering signatures (median Min85pct \sim 155 K). On the contrary, the median EL systems exhibit a relatively warm Min85pct (\sim 200 K).

The echo-top height of 35 dBZ (Maxht35), a proxy for the maximum height reached by graupel-sized particles, shows

similar patterns as the other convective proxies (Fig. 12c). BE exhibits a very robust mixed-phase process as indicated by its median echo-top height being higher than all others at roughly 10 km. NS exhibits a Maxht35 distribution just below that of BE, with a median Maxht35 of 9 km, indicating that NS storms also have a marked convective intensity. Most of the TS/LS and PS systems are indicated as being able to loft graupel-size ice particles (35 dBZ) well above the freezing level (8–9 km). Though weakest in intensity, EL systems still evidence of significant mixed-phase process (median Maxht35 of 6–7 km). Again, BE produces a high lightning flash rate (Fig. 12d), e.g., more than 50% and 20% of the BE storms reach intense (10 fl min^{-1}) and severe thunderstorm levels (50 fl min^{-1}), respectively. In contrast, only 15% of the EL systems produce a flash rate of 10 fl min^{-1} . NS induces a lower flash rate than BE, even though their Maxht35 is comparable, probably because the NS storms have a much smaller size than BE (Fig. 11a).

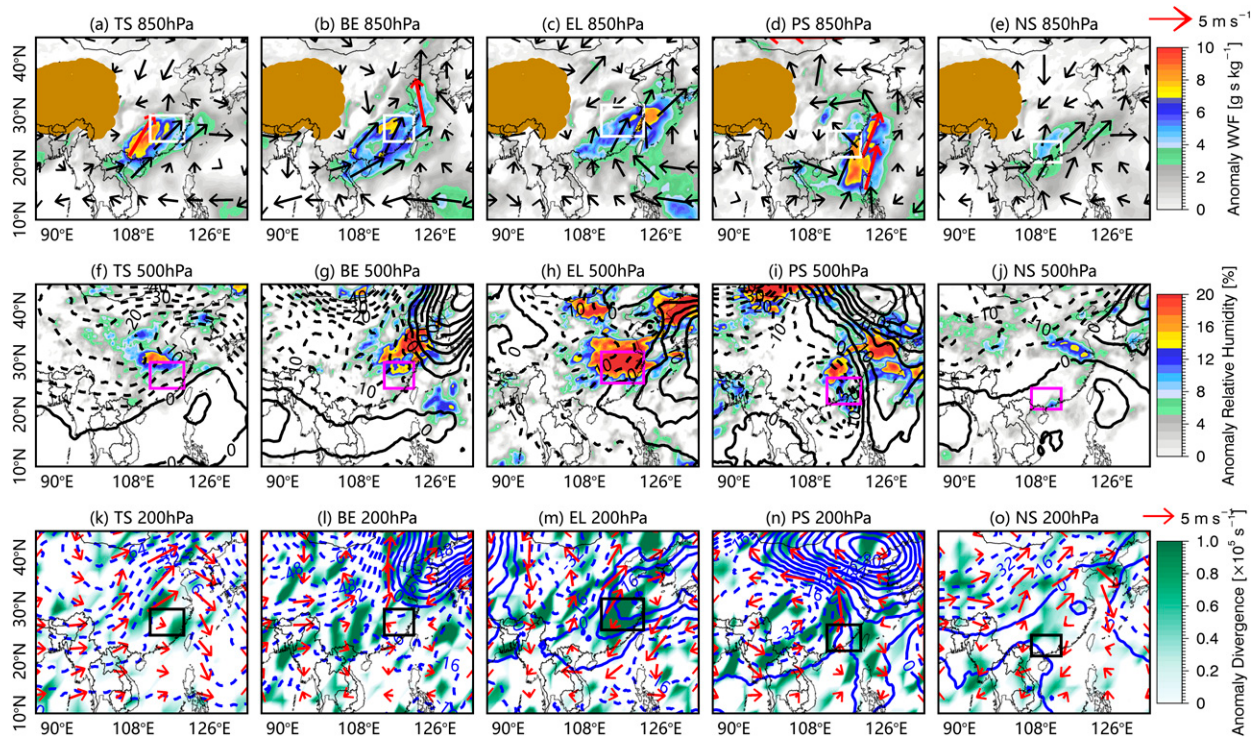


FIG. 10. As in Fig. 6, but for the linear MCSs in various organizational modes.

c. Vertical precipitation structure

Vertical precipitation structure of MCSs in China are the least known, especially for different modes of linear MCSs. Therefore, the vertical profiles of the TRMM PR reflectivity are composited as a function of LN organizational modes (Fig. 13). Obviously, BE and NS present the strongest vertical profiles of radar reflectivity, especially for the higher percentile profiles (e.g., 95th and 90th percentiles). The 95th–90th-percentile radar reflectivity profiles of BE and NS have 35–40 dBZ at 7–9 km altitudes (-10° to -25°C), indicating the presence of significant amount of large-size ice particles (graupel/hail) in the deep mixed-phase region induced by strong convection. Since the climatological warm-season freezing-level height over eastern China is 4.5–5.3 km (Guo et al. 2022), the 7–9 km altitudes have a temperature from -10° to -25°C , assuming a lapse rate of $6^{\circ}\text{--}7^{\circ}\text{C km}^{-1}$. The mixed-phase (7–9 km) echoes of TS and PS storms are 2–3 dBZ lower than those of the BE/NS, although their surface reflectivities are similar (<1 dBZ difference). The reflectivity lapse rates of the vertical profiles between 0° and -20°C (3 km interval above the freezing level) for BE/NS and TS/PS systems are -2.5 to -3.5 dBZ km^{-1} , close to those of typical continent convection (Zipser and Lutz 1994; Liu et al. 2008). Most of the TS/LS and PS systems are likely capable of lofting graupel-size particles well above the freezing level, based on observations of 35-dBZ echoes to 8–9 km. Though EL systems have the weakest vertical precipitation structure, they still show relatively strong reflectivity (30–35 dBZ) within the key mixed-phase region

($7\text{--}9$ km), suggesting active ice-based process. EL convection owns vertical profiles that decrease faster upward above the freezing level (-5 dBZ km^{-1}) compared to the other linear MCSs, likely due to a much weaker updraft (Zipser and Lutz 1994).

All linear MCS types show radar reflectivity profiles increasing downward (1–3 dBZ) below the melting level ($\sim 5\text{ km}$), indicating significant growth of rain drops through the warm-rain (collision-coalescence) process (Liu and Zipser 2013b; Zhao et al. 2022). The weaker the convective intensity, the greater downward increase of the radar reflectivity profiles, for instance, ~ 1 dBZ and 2–3 dBZ for the 95th–90th-percentile and 80th-percentile–median profiles, respectively. This is possibly because hydrometeors are more likely to fall through the weaker updrafts where cloud drops are abundant (supportive of active coalescence process), while most hydrometeors will fall out of strong updrafts leading to weaker coalescence process (Liu and Zipser 2013b). In short, vertical radar reflectivity profiles suggest that both ice-based and warm-rain processes play an important role in producing heavy precipitation of linear MCSs over China. The lack of increase in radar reflectivity with decreasing altitude in stronger convection cases may also result from the melting hail just beneath the melting layer, which could mask some of the signal of collisions–coalescence.

6. Summary and discussion

This study conducted a comprehensive investigation in MCSs over China (with the focus over south of 38°N), taking

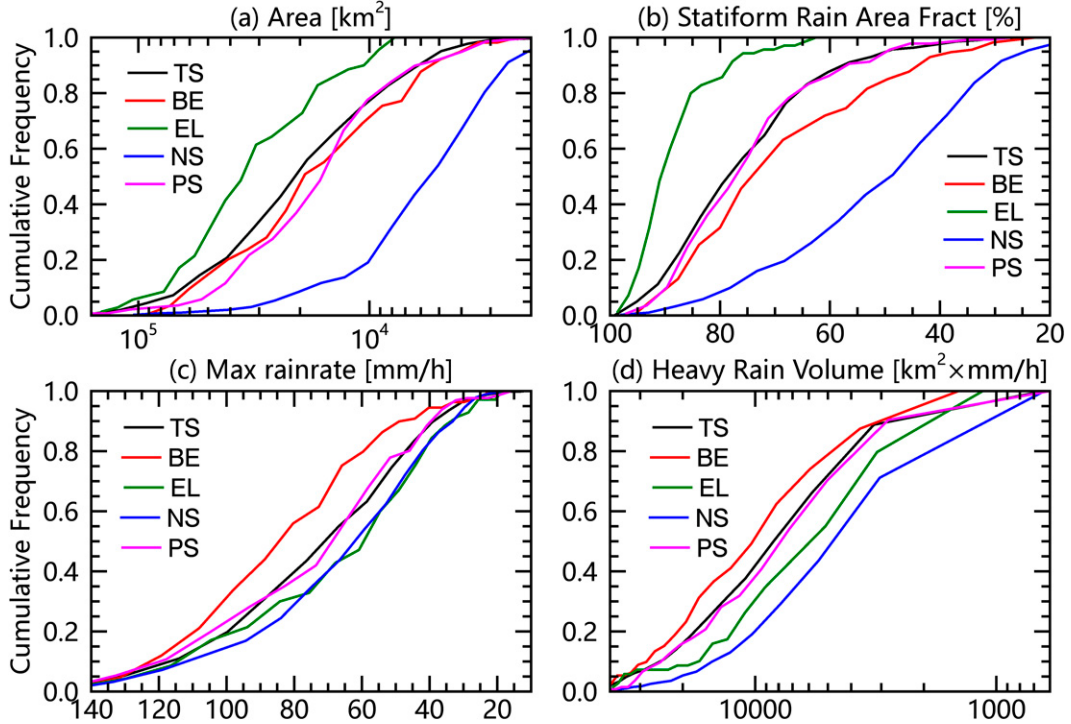


FIG. 11. As in Fig. 7, but for the linear MCSs in various organizational modes.

advantage of over 20 years of precipitation radar observations from TRMM and GPM satellites. The spatiotemporal variations, underlying large-scale environments, convective characteristics, and vertical precipitation structure of MCSs in various

organizational modes were extensively analyzed. The major findings of this study are summarized and discussed as follows.

First, the spatial-temporal distributions of MCSs in East Asia including China show a similar spatial pattern as

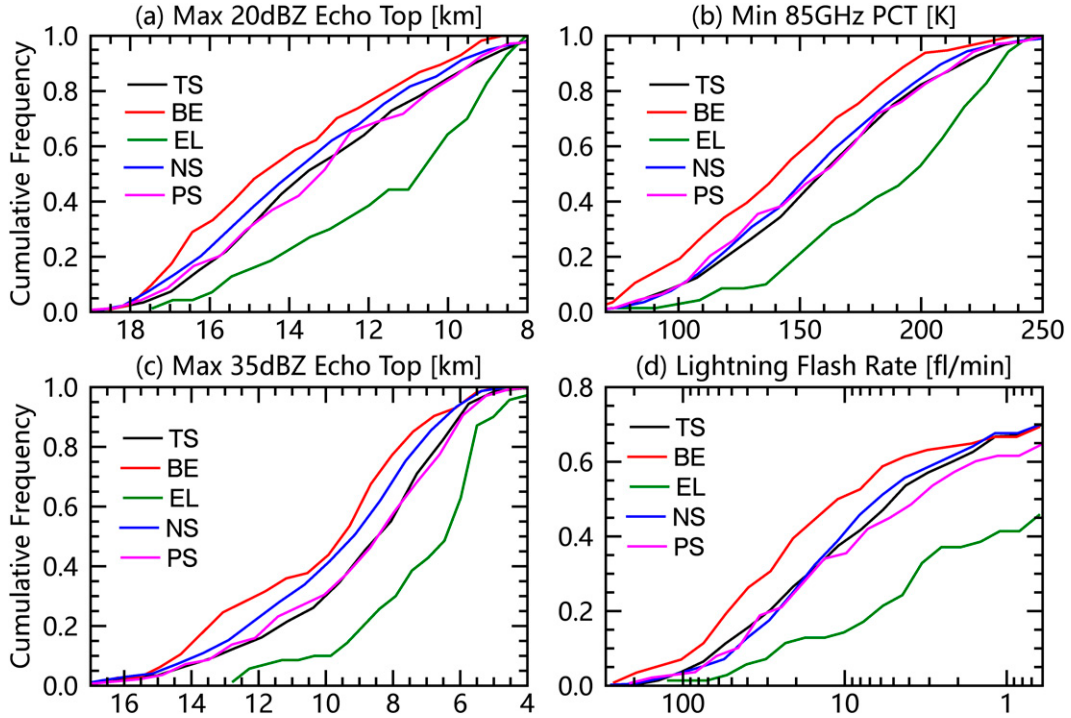


FIG. 12. As in Fig. 8, but for the linear MCSs in various organizational modes.

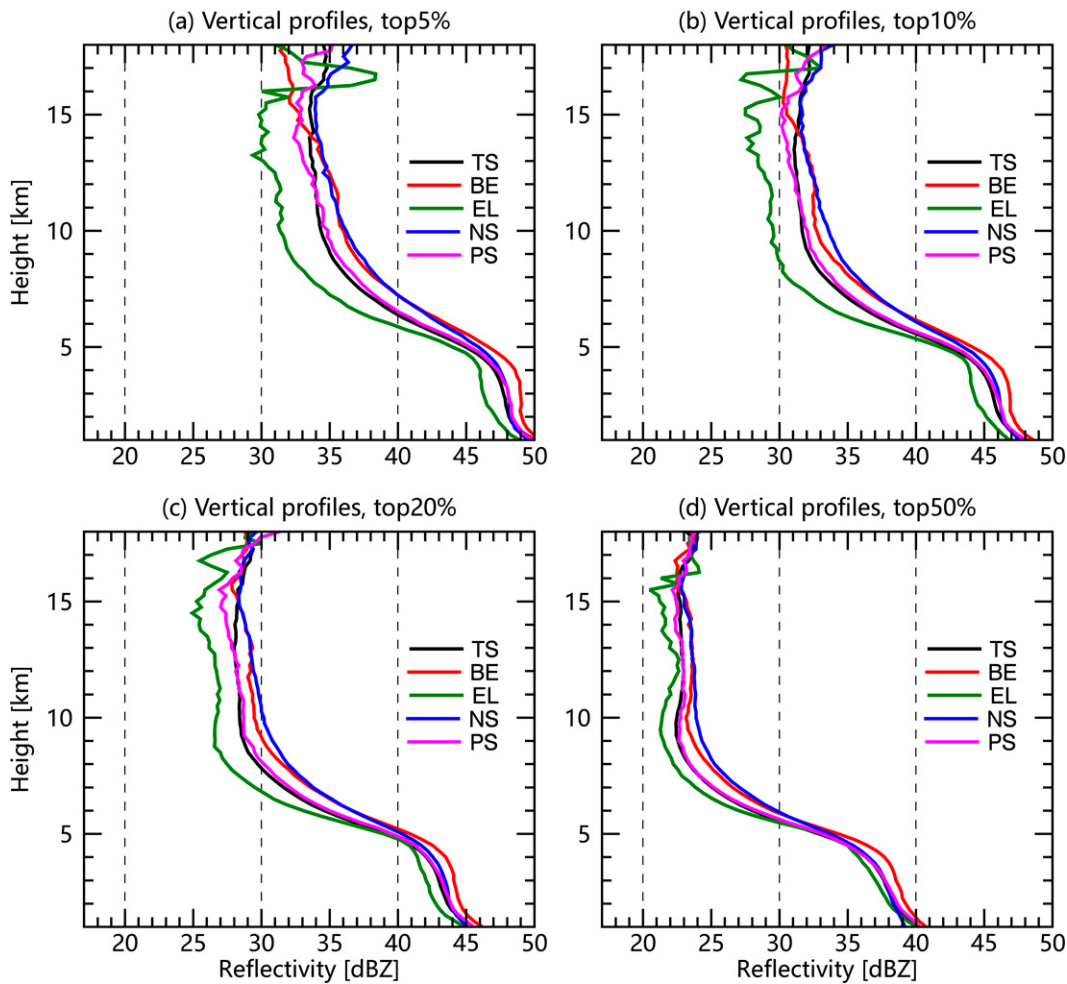


FIG. 13. Vertical profiles of radar reflectivity in convective regions of linear MCSs: the (a) 95th, (b) 90th, and (c) 80th percentiles and (d) the median. Different colors represent various organizational types of linear MCSs, including TS, BE, EL, NS, and PS.

precipitation, e.g., maximizing over the Yangtze River valley, the Wu-Yi Mountain areas, and southernmost China. The MCS frequency is at its minimum over the Tibetan Plateau, contrasting to the previously reported maximum in MCS activity over the southern Plateau using IR data (Zheng et al. 2008; Yang et al. 2015; Chen et al. 2019). This discrepancy is possibly because convective cloud systems over the Plateau have extensive and thick, cold cloud shields (thus detected by IR) but minimum precipitation down to the ground (not heavy enough to be detected as MCS by the spaceborne radar). The spaceborne radar-based climatology also better represents the mei-yu rainband, e.g., Figs. 2 and 3 compared to Fig. 3 in Zheng et al. (2008) and Fig. 6 in Yang et al. (2015), and its northward progression, exhibiting a more evident band-shaped feature and stronger seasonal migration pattern. On the diurnal scale, MCSs along the major mei-yu rainband (e.g., Yangtze River valley) are substantially enhanced (in terms of either frequency, size, or rain rate) in the early morning, possibly due to enhanced moisture convergence. Though

the MCS population over the southern China maximizes in the afternoon, their size and precipitation intensity still peak in the early morning, possibly due to precipitation enhancement by the nocturnally strengthened low-level jet over the upstream oceans.

Second, MCSs were categorized into linear MCSs (LNs) and nonlinear MCSs over the MCS-prone region in China. Only 17% of the MCSs (out of over 10 000) are linearly organized (LN), while more than 80% of them are nonlinear. The frequency and rainfall contribution of LN and BS are comparable to those of OTs, even though the OTs dominate the MCS population. While the occurrence frequency of nonlinear MCSs maximizes over the Wu-Yi Mountain and YZR areas, LNs are the most common over the northern China plains (to the north of the YZR) and the southernmost China. Linear MCSs are generally larger than nonlinear MCSs except BSs. BSs own the largest rain areas and the greatest fraction of stratiform precipitation, apparently due to greatly enhanced background wind shear and midtropospheric

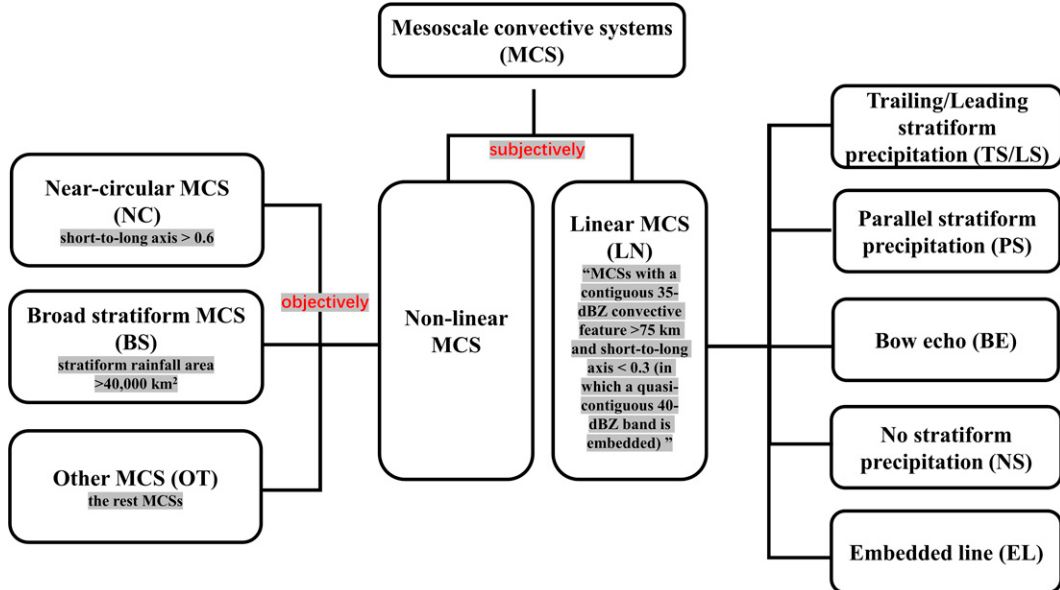


FIG. A1. Flowchart for identifying linear MCS and nonlinear MCS using near-surface reflectivity data from spaceborne radar. Both linear and nonlinear MCSs are further divided into subcategories.

moistest. All the TRMM convective proxies indicate that LNs have much stronger convection than nonlinear MCSs, emphasizing that LNs are more likely to induce severe weather (Zheng et al. 2013; Stevenson and Schumacher 2014; Cecil and Blankenship 2012). Though BSs have the weakest convective intensity, they induce a greater maximum rain rate and larger amount of heavy precipitation ($>10 \text{ mm h}^{-1}$) than other nonlinear MCSs. Thus, caution should be exercised by forecasters when considering the possibility of extreme rainfall and flooding due to BSs. LNs are associated with the most enhanced low-level flows ($\sim 10 \text{ m s}^{-1}$), the deepest midlevel trough and the strongest upper-level jets, as well as the greatest upper-level divergence. BSs show a similar large-scale condition as LNs but an even moister midtroposphere, suggesting some BSs are likely originated from LNs under a very moist midlevel condition.

Third, the convective and microphysical structure of linear MCSs in specific organizational modes were further explored, namely, trailing/leading stratiform (TS/LS), parallel stratiform (PS), bow echo (BE), no stratiform (NS), and embedded line (EL). TS and LS systems have the highest frequency (46.2%), followed by NS (28.3%), PS (10.5%), BE (8.7%), and EL (6.4%). BEs mainly occur under environments having enhanced low-level southwest flows, the deepest midlevel trough, and the largest CAPE ($\sim 1300 \text{ J kg}^{-1}$). Broader EL systems are mainly located to the north of $\sim 25^\circ \text{N}$, where significant vertical wind shear is also common. On the other hand, NS storms occur under the weakest large-scale dynamical forcing and are therefore, they are more likely thermally driven. As indicated by the radar reflectivity proxy of updraft strength (i.e., 35 dBZ echo-top height), BEs and NSs show the strongest convective intensity, ELs the weakest, and TS/LS in between. Though BEs and NSs both show the most vertically extended echo structure, strongest

microwave ice scattering, and highest lightning flash rates, NSs induce a much lower rain rate likely due to a drier environment. Most linear MCSs exhibit at least graupel-size hydrometeors in the deep mixed-phase regions (7–9 km), as indicated by the vertical radar reflectivity profiles. In addition, radar reflectivity profiles significantly increase downward below the melting height, suggesting that warm-rain process also play an important role in the precipitation processes of linear MCSs over China.

This study helps to better understand the convective organization, precipitation structure, and ensemble microphysical properties of MCSs over China, and potentially provides guidelines for evaluating high-resolution model simulations and satellite rainfall retrievals for monsoonal MCSs. To further understand the evolution of MCS structure, future work will consider the life cycle of MCSs. This could be done through combining spaceborne radar profiles, ground-based radar measurements, and satellite IR observations with high temporal resolution.

Acknowledgments. This research was supported by the National Key R&D Program of China (2019YFC1510400), the National Natural Science Foundation of China (41975053) and the Guangdong Provincial Department of Science and Technology, China (Grants 2019QN01G107, 2019ZT08G090). Special thanks go to the three anonymous reviewers for their constructive comments and suggestions.

Data availability statement. The TRMM and GPM data can be downloaded from the NASA Goddard Earth Sciences Data and Information Services Center (<http://disc.sci.gsfc.nasa.gov/TRMM>), and the ERA5 data can be accessed from the ECMWF (<https://www.ecmwf.int/en/forecasts/datasets/reanalysis-datasets/era5>).

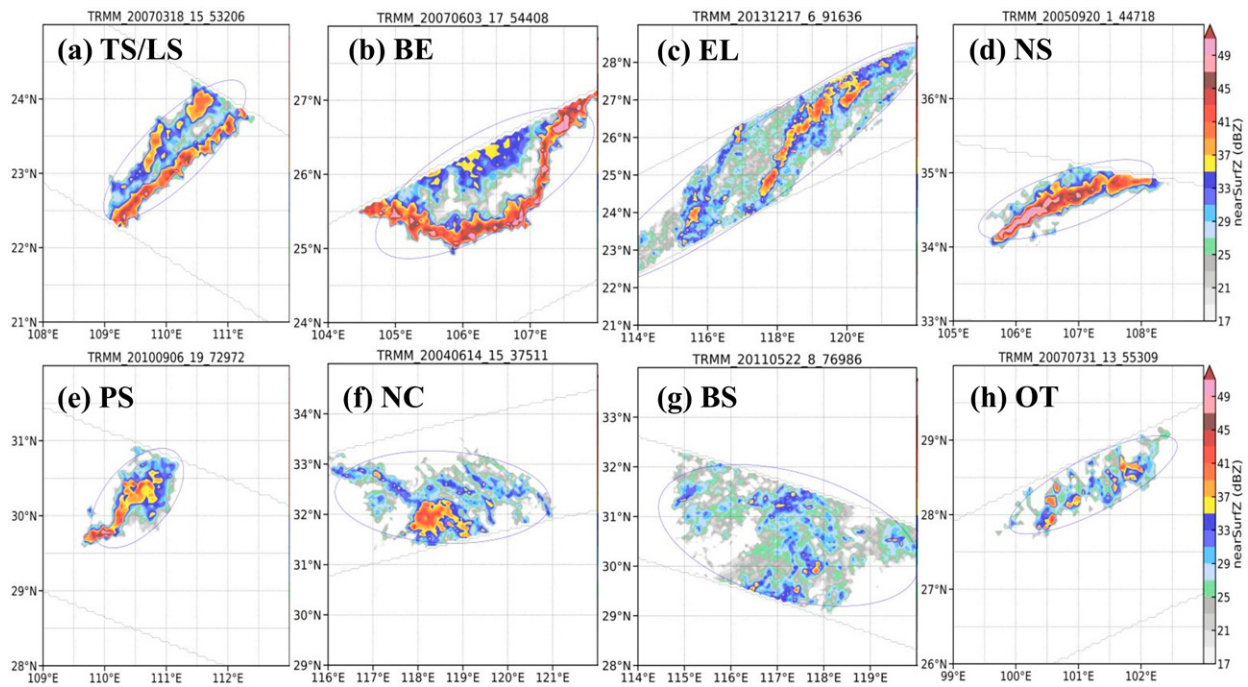


FIG. A2. Examples of linear MCSs in various organizational modes, including (a)–(e) linear MCSs and (f)–(h) nonlinear MCSs. Near-surface radar reflectivity is color shaded.

APPENDIX

Identifying and Categorizing MCSs

Figure A1 displays the flow chart for identifying and categorizing MCSs. Figure A2 shows the typical cases of MCSs in various organizational modes.

REFERENCES

- Ai, Y., W. Li, Z. Meng, and J. Li, 2016: Life cycle characteristics of MCSs in middle East China tracked by geostationary satellite and precipitation estimates. *Mon. Wea. Rev.*, **144**, 2517–2530, <https://doi.org/10.1175/MWR-D-15-0197.1>.
- Arkin, P. A., and B. N. Meisner, 1987: The relationship between large-scale convective rainfall and cold cloud over the Western Hemisphere during 1982–84. *Mon. Wea. Rev.*, **115**, 51–74, [https://doi.org/10.1175/1520-0493\(1987\)115<0051:TRBLSC>2.0.CO;2](https://doi.org/10.1175/1520-0493(1987)115<0051:TRBLSC>2.0.CO;2).
- Ashley, W. S., T. L. Mote, P. G. Dixon, S. L. Trotter, E. J. Powell, J. D. Durkee, and A. J. Grundstein, 2003: Distribution of mesoscale convective complex rainfall in the United States. *Mon. Wea. Rev.*, **131**, 3003–3017, [https://doi.org/10.1175/1520-0493\(2003\)131<3003:DOMCCR>2.0.CO;2](https://doi.org/10.1175/1520-0493(2003)131<3003:DOMCCR>2.0.CO;2).
- , A. M. Haberlie, and J. Strohm, 2019: A climatology of quasi-linear convective systems and their hazards in the United States. *Wea. Forecasting*, **34**, 1605–1631, <https://doi.org/10.1175/WAF-D-19-0014.1>.
- Bao, X., F. Zhang, and J. Sun, 2011: Diurnal variations of warm-season precipitation east of the Tibetan Plateau over China. *Mon. Wea. Rev.*, **139**, 2790–2810, <https://doi.org/10.1175/MWR-D-11-00006.1>.
- Carbone, R. E., and J. D. Tuttle, 2008: Rainfall occurrence in the U.S. warm season: The diurnal cycle. *J. Climate*, **21**, 4132–4146, <https://doi.org/10.1175/2008JCLI2275.1>.
- Cecil, D. J., and C. B. Blankenship, 2012: Toward a global climatology of severe hailstorms as estimated by satellite passive microwave imagers. *J. Climate*, **25**, 687–703, <https://doi.org/10.1175/JCLI-D-11-00130.1>.
- , S. J. Goodman, D. J. Boccippio, E. J. Zipser, and S. W. Nesbitt, 2005: Three years of TRMM precipitation features. Part I: Radar, radiometric, and lightning characteristics. *Mon. Wea. Rev.*, **133**, 543–566, <https://doi.org/10.1175/MWR-2876.1>.
- Chen, D., and Coauthors, 2019: Mesoscale convective systems in the Asian monsoon region from Advanced Himawari Imager: Algorithms and preliminary results. *J. Geophys. Res. Atmos.*, **124**, 2210–2234, <https://doi.org/10.1029/2018JD029707>.
- Chen, X., K. Zhao, and M. Xue, 2014: Spatial and temporal characteristics of warm season convection over Pearl River Delta region, China, based on 3 years of operational radar data. *J. Geophys. Res. Atmos.*, **119**, 12 447–12 465, <https://doi.org/10.1002/2014JD021965>.
- Cui, W., X. Dong, B. Xi, and M. Liu, 2020: Cloud and precipitation properties of MCSs along the Meiyu frontal zone in central and southern China and their associated large-scale environments. *J. Geophys. Res. Atmos.*, **125**, e2019JD031601, <https://doi.org/10.1029/2019JD031601>.
- , —, —, and Z. Feng, 2021: Climatology of linear mesoscale convective system morphology in the United States based on the random-forests method. *J. Climate*, **34**, 7257–7276, <https://doi.org/10.1175/JCLI-D-20-0862.1>.
- Ding, Y., 2007: The variability of the Asian summer monsoon. *J. Meteor. Soc. Japan*, **85B**, 21–54, <https://doi.org/10.2151/jmsj.85B.21>.

- , and J. C. L. Chan, 2005: The East Asian summer monsoon: An overview. *Meteor. Atmos. Phys.*, **89**, 117–142, <https://doi.org/10.1007/s00703-005-0125-z>.
- Du, Y., G. Chen, B. Han, L. Bai, and M. Li, 2020: Convection initiation and growth at the coast of South China. Part II: Effects of the terrain, coastline, and cold pools. *Mon. Wea. Rev.*, **148**, 3871–3892, <https://doi.org/10.1175/MWR-D-20-0090.1>.
- Feng, Z., L. R. Leung, S. Hagos, R. A. Houze, C. D. Burleyson, and K. Balaguru, 2016: More frequent intense and long-lived storms dominate the springtime trend in central U.S. rainfall. *Nat. Commun.*, **7**, 13429, <https://doi.org/10.1038/ncomms13429>.
- , R. A. Houze Jr., L. R. Leung, F. Song, J. C. Hardin, J. Wang, W. I. Gustafson Jr., and C. R. Homeyer, 2019: Spatiotemporal characteristics and large-scale environments of mesoscale convective systems east of the Rocky Mountains. *J. Climate*, **32**, 7303–7328, <https://doi.org/10.1175/JCLI-D-19-0137.1>.
- , and Coauthors, 2021: A global high-resolution mesoscale convective system database using satellite-derived cloud tops, surface precipitation, and tracking. *J. Geophys. Res. Atmos.*, **126**, e2020JD034202, <https://doi.org/10.1029/2020JD034202>.
- Fritsch, J. M., R. J. Kane, and C. R. Chelius, 1986: The contribution of mesoscale convective weather systems to the warm-season precipitation in the United States. *J. Climate Appl. Meteor.*, **25**, 1333–1345, [https://doi.org/10.1175/1520-0450\(1986\)025<1333:TCOMCW>2.0.CO;2](https://doi.org/10.1175/1520-0450(1986)025<1333:TCOMCW>2.0.CO;2).
- Gallus, W. A., Jr., N. A. Snook, and E. V. Johnson, 2008: Spring and summer severe weather reports over the Midwest as a function of convective mode: A preliminary study. *Wea. Forecasting*, **23**, 101–113, <https://doi.org/10.1175/2007WAF2006120.1>.
- Geng, B., and H. Yamada, 2007: Diurnal variations of the Meiyu/Baiu rain belt. *SOLA*, **3**, 61–64, <https://doi.org/10.2151/sola.2007-016>.
- Guan, P., G. Chen, W. Zeng, and Q. Liu, 2020: Corridors of meiyu-season rainfall over eastern China. *J. Climate*, **33**, 2603–2626, <https://doi.org/10.1175/JCLI-D-19-0649.1>.
- Guastini, C. T., and L. F. Bosart, 2016: Analysis of a progressive derecho climatology and associated formation environments. *Mon. Wea. Rev.*, **144**, 1363–1382, <https://doi.org/10.1175/MWR-D-15-0256.1>.
- Guo, Y., G. Wang, and Q. Chao, 2022: Climatological analysis of freezing level height over China and its implications using homogenized in-situ data. *Int. J. Climatol.*, **42**, 559–576, <https://doi.org/10.1002/joc.7260>.
- Haberlie, A. M., and W. S. Ashley, 2019: A radar-based climatology of mesoscale convective systems in the United States. *J. Climate*, **32**, 1591–1606, <https://doi.org/10.1175/JCLI-D-18-0559.1>.
- Hamada, A., and Y. N. Takayabu, 2014: A removal filter for suspicious extreme rainfall profiles in TRMM PR 2A25 version-7 data. *J. Appl. Meteor. Climatol.*, **53**, 1252–1271, <https://doi.org/10.1175/JAMC-D-13-099.1>.
- He, Z., Q. Zhang, and J. Sun, 2016: The contribution of mesoscale convective systems to intense hourly precipitation events during the warm seasons over central East China. *Adv. Atmos. Sci.*, **33**, 1233–1239, <https://doi.org/10.1007/s00376-016-6034-x>.
- Hersbach, H., and Coauthors, 2020: The ERA5 global reanalysis. *Quart. J. Roy. Meteor. Soc.*, **146**, 1999–2049, <https://doi.org/10.1002/qj.3803>.
- Houze, R. A., Jr., 2018: 100 years of research on mesoscale convective systems. *A Century of Progress in Atmospheric and Related Sciences: Celebrating the American Meteorological Society Centennial*, Meteor. Monogr., No. 59, Amer. Meteor. Soc., 17.1–17.54, <https://doi.org/10.1175/AMSMONOGRAPHSD-18-0001.1>.
- , B. F. Smull, and P. Dodge, 1990: Mesoscale organization of springtime rainstorms in Oklahoma. *Mon. Wea. Rev.*, **118**, 613–654, [https://doi.org/10.1175/1520-0493\(1990\)118<0613:MOOSRI>2.0.CO;2](https://doi.org/10.1175/1520-0493(1990)118<0613:MOOSRI>2.0.CO;2).
- , D. C. Wilton, and B. F. Smull, 2007: Monsoon convection in the Himalayan region as seen by the TRMM Precipitation Radar. *Quart. J. Roy. Meteor. Soc.*, **133**, 1389–1411, <https://doi.org/10.1002/qj.106>.
- , K. L. Rasmussen, M. D. Zuluaga, and S. R. Brodzik, 2015: The variable nature of convection in the tropics and subtropics: A legacy of 16 years of the Tropical Rainfall Measuring Mission satellite. *Rev. Geophys.*, **53**, 994–1021, <https://doi.org/10.1002/2015RG000488>.
- Iguchi, T., T. Kozu, R. Meneghini, J. Awaka, and K. Okamoto, 2000: Rain-profiling algorithm for the TRMM Precipitation Radar. *J. Appl. Meteor.*, **39**, 2038–2052, [https://doi.org/10.1175/1520-0450\(2001\)040<2038:RPAFTT>2.0.CO;2](https://doi.org/10.1175/1520-0450(2001)040<2038:RPAFTT>2.0.CO;2).
- , and Coauthors, 2021: GPM/DPR level-2 algorithm theoretical basis document, version V07A. JAXA Earth Observation Research Center, 238 pp., https://www.eorc.jaxa.jp/GPM/doc/algorith/ATBD_DPR_V07A.pdf.
- Johnson, R. H., S. L. Aves, P. E. Ciesielski, and T. D. Keenan, 2005: Organization of oceanic convection during the onset of the 1998 East Asian summer monsoon. *Mon. Wea. Rev.*, **133**, 131–148, <https://doi.org/10.1175/MWR-2843.1>.
- Li, P., C. Moseley, A. F. Prein, H. Chen, J. Li, K. Furtado, and T. Zhou, 2020: Mesoscale convective system precipitation characteristics over East Asia. Part I: Regional differences and seasonal variations. *J. Climate*, **33**, 9271–9286, <https://doi.org/10.1175/JCLI-D-20-0072.1>.
- Lin, G., C. Grasmick, B. Geerts, Z. Wang, and M. Deng, 2021: Convection initiation and bore formation following the collision of mesoscale boundaries over a developing stable boundary layer: A case study from PEACAN. *Mon. Wea. Rev.*, **149**, 2351–2367, <https://doi.org/10.1175/MWR-D-20-0282.1>.
- Liu, C., and E. J. Zipser, 2013a: Regional variation of morphology of organized convection in the tropics and subtropics. *J. Geophys. Res. Atmos.*, **118**, 453–466, <https://doi.org/10.1029/2012JD018409>.
- , and —, 2013b: Why does radar reflectivity tend to increase downward toward the ocean surface, but decrease downward toward the land surface? *J. Geophys. Res. Atmos.*, **118**, 135–148, <https://doi.org/10.1029/2012JD018134>.
- , —, D. J. Cecil, S. W. Nesbitt, and S. Sherwood, 2008: A cloud and precipitation feature database from nine years of TRMM observations. *J. Appl. Meteor. Climatol.*, **47**, 2712–2728, <https://doi.org/10.1175/2008JAMC1890.1>.
- , S. Shige, Y. N. Takayabu, and E. Zipser, 2015: Latent heating contribution from precipitation systems with different sizes, depths, and intensities in the tropics. *J. Climate*, **28**, 186–203, <https://doi.org/10.1175/JCLI-D-14-00370.1>.
- Liu, D., M. Sun, D. Su, W. Xu, H. Yu, and Y. Chen, 2021: A five-year climatological lightning characteristics of linear mesoscale convective systems over North China. *Atmos. Res.*, **256**, 105580, <https://doi.org/10.1016/j.atmosres.2021.105580>.
- Liu, N., and C. Liu, 2016: Global distribution of deep convection reaching tropopause in 1 year GPM observations. *J. Geophys. Res. Atmos.*, **121**, 3824–3842, <https://doi.org/10.1002/2015JD024430>.
- Luo, Y., H. Wang, R. Zhang, W. Qian, and Z. Luo, 2013: Comparison of rainfall characteristics and convective properties of

- monsoon precipitation systems over South China and the Yangtze and Huai River basin. *J. Climate*, **26**, 110–132, <https://doi.org/10.1175/JCLI-D-12-00100.1>.
- Ma, R., J. Sun, and X. Yang, 2021: A 7-yr climatology of the initiation, decay, and morphology of severe convective storms during the warm season over North China. *Mon. Wea. Rev.*, **149**, 2599–2612, <https://doi.org/10.1175/MWR-D-20-0087.1>.
- Mai, Z., S.-M. Fu, J.-H. Sun, L. Hu, and X.-M. Wang, 2021: Key statistical characteristics of the mesoscale convective systems generated over the Tibetan Plateau and their relationship to precipitation and southwest vortices. *Int. J. Climatol.*, **41**, E875–E896, <https://doi.org/10.1002/joc.6735>.
- Meng, Y., J. Sun, Y. Zhang, and S. Fu, 2021: A 10-year climatology of mesoscale convective systems and their synoptic circulations in the southwest mountain area of China. *J. Hydrometeor.*, **22**, 23–41, <https://doi.org/10.1175/JHM-D-20-0167.1>.
- Meng, Z., D. Yan, and Y. Zhang, 2013: General features of squall lines in East China. *Mon. Wea. Rev.*, **141**, 1629–1647, <https://doi.org/10.1175/MWR-D-12-00208.1>.
- , and Coauthors, 2018: The deadliest tornado (EF4) in the past 40 years in China. *Wea. Forecasting*, **33**, 693–713, <https://doi.org/10.1175/WAF-D-17-0085.1>.
- Moncrieff, M. W., 2010: The multiscale organization of moist convection and the intersection of weather and climate. *Climate Dynamics: Why Does Climate Vary*, D.-Z. Sun and F. Bryan, Eds., Vol. 189, Amer. Geophys. Union, 3–26.
- Nesbitt, S. W., and A. M. Anders, 2009: Very high resolution precipitation climatologies from the Tropical Rainfall Measuring Mission Precipitation Radar. *Geophys. Res. Lett.*, **36**, L15815, <https://doi.org/10.1029/2009GL038026>.
- , E. J. Zipser, and D. J. Cecil, 2000: A census of precipitation features in the tropics using TRMM: Radar, ice scattering, and lightning observations. *J. Climate*, **13**, 4087–4106, [https://doi.org/10.1175/1520-0442\(2000\)013<4087:ACOPFI>2.0.CO;2](https://doi.org/10.1175/1520-0442(2000)013<4087:ACOPFI>2.0.CO;2).
- , R. Cifelli, and S. A. Rutledge, 2006: Storm morphology and rainfall characteristics of TRMM precipitation features. *Mon. Wea. Rev.*, **134**, 2702–2721, <https://doi.org/10.1175/MWR3200.1>.
- Parker, M. D., and R. H. Johnson, 2000: Organizational modes of midlatitude mesoscale convective systems. *Mon. Wea. Rev.*, **128**, 3413–3436, [https://doi.org/10.1175/1520-0493\(2001\)129<3413:OMOMMC>2.0.CO;2](https://doi.org/10.1175/1520-0493(2001)129<3413:OMOMMC>2.0.CO;2).
- Prein, A. F., C. Liu, K. Ikeda, S. B. Trier, R. M. Rasmussen, G. J. Holland, and M. P. Clark, 2017: Increased rainfall volume from future convective storms in the U.S. *Nat. Climate Change*, **7**, 880–884, <https://doi.org/10.1038/s41558-017-0007-7>.
- Rasmussen, K. L., A. F. Prein, R. M. Rasmussen, K. Ikeda, and C. Liu, 2020: Changes in the convective population and thermodynamic environments in convection-permitting regional climate simulations over the United States. *Climate Dyn.*, **55**, 383–408, <https://doi.org/10.1007/s00382-017-4000-7>.
- Rickenbach, T. M., 1999: Cloud-top evolution of tropical oceanic squall lines from radar reflectivity and infrared satellite data. *Mon. Wea. Rev.*, **127**, 2951–2976, [https://doi.org/10.1175/1520-0493\(1999\)127<2951:CTEOTO>2.0.CO;2](https://doi.org/10.1175/1520-0493(1999)127<2951:CTEOTO>2.0.CO;2).
- Schenkman, A. D., and M. Xue, 2016: Bow-echo mesovortices: A review. *Atmos. Res.*, **170**, 1–13, <https://doi.org/10.1016/j.atmosres.2015.11.003>.
- Schumacher, R. S., and R. H. Johnson, 2005: Organization and environmental properties of extreme-rain-producing mesoscale convective systems. *Mon. Wea. Rev.*, **133**, 961–976, <https://doi.org/10.1175/MWR2899.1>.
- , and —, 2006: Characteristics of U.S. extreme rain events during 1999–2003. *Wea. Forecasting*, **21**, 69–85, <https://doi.org/10.1175/WAF900.1>.
- , and K. L. Rasmussen, 2020: The formation, character and changing nature of mesoscale convective systems. *Nat. Rev. Earth Environ.*, **1**, 300–314, <https://doi.org/10.1038/s43017-020-0057-7>.
- Seto, S., and T. Iguchi, 2015: Intercomparison of attenuation correction methods for the GPM dual-frequency precipitation radar. *J. Atmos. Oceanic Technol.*, **32**, 915–926, <https://doi.org/10.1175/JTECH-D-14-00065.1>.
- Stensrud, D. J., 1996: Effects of persistent, midlatitude mesoscale regions of convection on the large-scale environment during the warm season. *J. Atmos. Sci.*, **53**, 3503–3527, [https://doi.org/10.1175/1520-0469\(1996\)053<3503:EOPMMR>2.0.CO;2](https://doi.org/10.1175/1520-0469(1996)053<3503:EOPMMR>2.0.CO;2).
- Stevenson, S. N., and R. S. Schumacher, 2014: A 10-year survey of extreme rainfall events in the central and eastern United States using gridded multisensor precipitation analyses. *Mon. Wea. Rev.*, **142**, 3147–3162, <https://doi.org/10.1175/MWR-D-13-00345.1>.
- Sun, J., and F. Zhang, 2012: Impacts of mountain–plains solenoid on diurnal variations of rainfalls along the mei-yu front over the East China plains. *Mon. Wea. Rev.*, **140**, 379–397, <https://doi.org/10.1175/MWR-D-11-00041.1>.
- Sun, Y., X. Dong, W. Cui, Z. Zhou, Z. Fu, L. Zhou, Y. Deng, and C. Cui, 2020: Vertical structures of typical Meiyu precipitation events retrieved from GPM-DPR. *J. Geophys. Res. Atmos.*, **125**, e2019JD031466, <https://doi.org/10.1029/2019JD031466>.
- Taylor, C. M., and Coauthors, 2017: Frequency of extreme Sahelian storms tripled since 1982 in satellite observations. *Nature*, **544**, 475–478, <https://doi.org/10.1038/nature22069>.
- Wang, B., 2006: *The Asian Monsoon*. Springer Science and Business Media, 787 pp.
- Wang, H., Y. Luo, and B. J.-D. Jou, 2014: Initiation, maintenance, and properties of convection in an extreme rainfall event during SCMREX: Observational analysis. *J. Geophys. Res. Atmos.*, **119**, 13 206–13 232, <https://doi.org/10.1002/2014JD022339>.
- Wang, J., R. A. Houze Jr., J. Fan, S. R. Brodzik, Z. Feng, and J. C. Hardin, 2019: The detection of mesoscale convective systems by the GPM Ku-band spaceborne radar. *J. Meteor. Soc. Japan*, **97**, 1059–1073, <https://doi.org/10.2151/jmsj.2019-058>.
- Wang, T., and G. Tang, 2020: Spatial variability and linkage between extreme convective and extreme precipitation revealed by 22-year space-borne precipitation radar data. *Geophys. Res. Lett.*, **47**, e2020GL088437, <https://doi.org/10.1029/2020GL088437>.
- Wang, X., C. Cui, W. Cui, and Y. Shi, 2014: Modes of mesoscale convective system organization during Meiyu season over the Yangtze River basin. *J. Meteor. Res.*, **28**, 111–126, <https://doi.org/10.1007/s13351-014-0108-4>.
- Weisman, M. L., 1993: The genesis of severe, long-lived bow echoes. *J. Atmos. Sci.*, **50**, 645–670, [https://doi.org/10.1175/1520-0469\(1993\)050<0645:TGOSLL>2.0.CO;2](https://doi.org/10.1175/1520-0469(1993)050<0645:TGOSLL>2.0.CO;2).
- Xia, R., D. Wang, J. Sun, G. Wang, and G. Xia, 2012: An observational analysis of a derecho in South China. *Acta Meteor. Sin.*, **26**, 773–787, <https://doi.org/10.1007/s13351-012-0608-z>.
- Xie, B., Q. Zhang, and Y. Wang, 2010: Observed characteristics of hail size in four regions in China during 1980–2005. *J. Climate*, **23**, 4973–4982, <https://doi.org/10.1175/2010JCLI3600.1>.
- Xu, W., 2013: Precipitation and convective characteristics of summer deep convection over East Asia observed by TRMM. *Mon. Wea. Rev.*, **141**, 1577–1592, <https://doi.org/10.1175/MWR-D-12-00177.1>.

- , 2020: Thunderstorm climatologies and their relationships to total and extreme precipitation in China. *J. Geophys. Res. Atmos.*, **125**, e2020JD033152, <https://doi.org/10.1029/2020JD033152>.
- , and E. J. Zipser, 2011: Diurnal variations of precipitation, deep convection and lightning over and east of the eastern Tibetan Plateau. *J. Climate*, **24**, 448–465, <https://doi.org/10.1175/2010JCLI3719.1>.
- , and —, 2012: Properties of deep convection in tropical continental, monsoon, and oceanic rainfall regimes. *Geophys. Res. Lett.*, **39**, L07802, <https://doi.org/10.1029/2012GL051242>.
- , —, and C. Liu, 2009: Rainfall characteristics and convective properties of mei-yu precipitation systems over South China, Taiwan, and the South China Sea. Part I: TRMM observations. *Mon. Wea. Rev.*, **137**, 4261–4275, <https://doi.org/10.1175/2009MWR2982.1>.
- Yang, R., Y. Zhang, J. Sun, S. Fu, and J. Li, 2018: The characteristics and classification of eastward-propagating mesoscale convective systems generated over the second-step terrain in the Yangtze River Valley. *Atmos. Sci. Lett.*, **20**, e874, <https://doi.org/10.1002/asl.874>.
- Yang, X., and J. Sun, 2018: Organizational modes of severe wind-producing convective systems over North China. *Adv. Atmos. Sci.*, **35**, 540–549, <https://doi.org/10.1007/s00376-017-7114-2>.
- , J. Fei, X. Huang, X. Cheng, L. M. V. Carvalho, and H. He, 2015: Characteristics of mesoscale convective systems over China and its vicinity using geostationary satellite FY2. *J. Climate*, **28**, 4890–4907, <https://doi.org/10.1175/JCLI-D-14-00491.1>.
- Zhang, C., Q. Zhang, and Y. Wang, 2008: Climatology of hail in China: 1961–2005. *J. Appl. Meteor. Climatol.*, **47**, 795–804, <https://doi.org/10.1175/2007JAMC1603.1>.
- Zhang, L., J. Min, X. Zhuang, and R. S. Schumacher, 2019: General features of extreme rainfall events produced by MCSs over East China during 2016–17. *Mon. Wea. Rev.*, **147**, 2693–2714, <https://doi.org/10.1175/MWR-D-18-0455.1>.
- Zhang, X., W. Shen, X. Zhuge, S. Yang, Y. Chen, Y. Wang, T. Chen, and S. Zhang, 2021: Statistical characteristics of meso-scale convective systems initiated over the Tibetan Plateau in summer by Fengyun satellite and precipitation estimates. *Remote Sens.*, **13**, 1652, <https://doi.org/10.3390/rs13091652>.
- Zhang, Y., F. Zhang, and J. Sun, 2014: Comparison of the diurnal variations of warm-season precipitation for East Asia vs. North America downstream of the Tibetan Plateau vs. the Rocky Mountains. *Atmos. Chem. Phys.*, **14**, 10741–10759, <https://doi.org/10.5194/acp-14-10741-2014>.
- Zheng, L., J. Sun, X. Zhang, and C. Liu, 2013: Organizational modes of mesoscale convective systems over central East China. *Wea. Forecasting*, **28**, 1081–1098, <https://doi.org/10.1175/WAF-D-12-00088.1>.
- Zheng, Y., J. Chen, and P. Zhu, 2008: Climatological distribution and diurnal variation of mesoscale convective systems over China and its vicinity during summer. *Chin. Sci. Bull.*, **53**, 1574–1586, <https://doi.org/10.1007/s11434-008-0116-9>.
- Zhao, D., W. Gao, H. Xu, Y. Yu, and L. Chen, 2022: A modeling study of cloud physical properties of extreme and non-extreme precipitation in landfalling typhoons over China. *Atmos. Res.*, **277**, 106311, <https://doi.org/10.1016/j.atmosres.2022.106311>.
- Zhou, T., R. Yu, H. Chen, A. Dai, and Y. Pan, 2008: Summer precipitation frequency, intensity, and diurnal cycle over China: A comparison of satellite data with rain gauge observations. *J. Climate*, **21**, 3997–4010, <https://doi.org/10.1175/2008JCLI2028.1>.
- Zipser, E. J., and K. R. Lutz, 1994: The vertical profile of radar reflectivity of convective cells: A strong indicator of storm intensity and lightning probability? *Mon. Wea. Rev.*, **122**, 1751–1759, [https://doi.org/10.1175/1520-0493\(1994\)122<1751:TVPORR>2.0.CO;2](https://doi.org/10.1175/1520-0493(1994)122<1751:TVPORR>2.0.CO;2).
- , D. J. Cecil, C. Liu, S. W. Nesbitt, and D. P. Yorty, 2006: Where are the most intense thunderstorms on Earth? *Bull. Amer. Meteor. Soc.*, **87**, 1057–1072, <https://doi.org/10.1175/BAMS-87-8-1057>.